

Visual-Inertial SLAM as Simple as A, B, VINS

Nathaniel Merrill and Guoquan Huang

Abstract—We present AB-VINS, a different kind of visual-inertial SLAM system. Unlike most VINS systems which only use hand-crafted techniques, AB-VINS makes use of three different deep networks. Instead of estimating sparse feature positions, AB-VINS only estimates the scale and bias parameters (a and b) of monocular depth maps, as well as other terms to correct the depth using multi-view information which results in a compressed feature state. Despite being an optimization-based system, the main VIO thread of AB-VINS surpasses the efficiency of a state-of-the-art filter-based method while also providing dense depth. While state-of-the-art loop-closing SLAM systems have to relinearize a number of variables linear the number of keyframes, AB-VINS can perform loop closures while only affecting a constant number of variables. This is due to a novel data structure called the memory tree, in which the keyframe poses are defined relative to each other rather than all in one global frame, allowing for all but a few states to be fixed. AB-VINS is not as accurate as state-of-the-art VINS systems, but it is shown through careful experimentation to be more robust.

I. INTRODUCTION

Visual-inertial simultaneous localization and mapping (SLAM) systems are crucial for augmented reality (AR) and virtual reality (VR). Leveraging the complimentary camera and inertial measurement unit (IMU) measurements, such systems output the high-rate metric, gravity-aligned poses (position and orientation) required for rendering, and bound the pose estimation error over time by remembering places they have been – performing loop closures to past states in order to prevent the user from drifting away in the virtual world. Besides the poses, dense depth is also useful for AR specifically. It is helpful for creating the illusion of occlusion with rendered objects, and it creates a solid surface for virtual characters to interact with.

Besides AR/VR, poses paired with dense depth are also needed for many robotic applications, such as obstacle avoidance and path planning. Despite the need for dense depth, very few VINS systems actually provide it. Additionally, despite recent advances in deep learning for a multitude of related applications, very few VINS systems have actually utilized deep networks. The proposed AB-VINS on the other hand provides high-rate gravity-aligned poses along with dense depth, and uses three different deep networks to its advantage. Visual-inertial SLAM needs to be as efficient as possible, being able to quickly close loops while running on some of the smallest devices – even as small as a bee robot in future applications. AB-VINS contains, to the best of our knowledge, the most efficient pose graph SLAM solution ever proposed thanks to the novel memory tree, which brings us one step

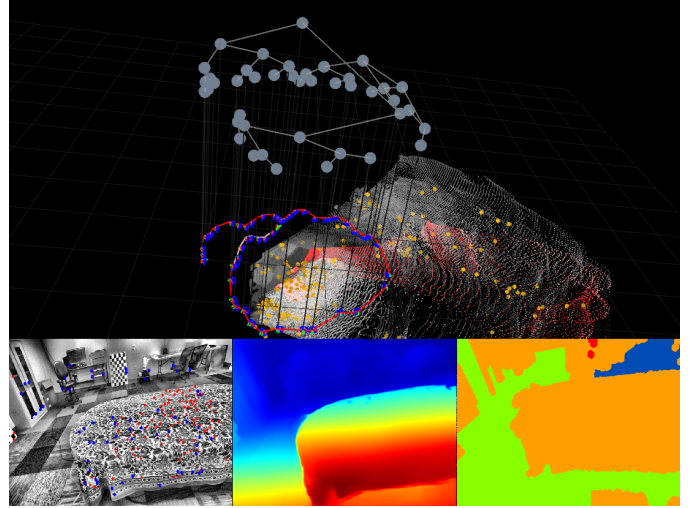


Fig. 1: A snapshot of the AB-VINS visualizer gives an overview of our system. On the bottom left is the current frame with feature tracks (red) and reprojected points (blue) overlaid. On the bottom center is the most recent keyframe depth map. On the bottom right is the code mask, which divides the images into different regions that are pushed and pulled to correct the depth according to multi-view information. In the main window at the top the memory tree can be seen, which is a novel data structure used to speed up pose graph optimization.

closer to achieving such goals. An overview of AB-VINS can be seen in Fig. 1. Our main contributions are:

- A new monocular visual-inertial SLAM system AB-VINS is proposed, which exhibits state-of-the-art robustness and efficiency while also providing dense depth.
- A compact feature representation called AB features is presented, where an arbitrary number of feature positions are parameterized by a and b , the scale and bias of a monocular depth map, as well as other terms to correct the depth with multi-view information.
- The memory tree, a novel data structure used to significantly speed up pose graph optimization, is introduced. The memory tree allows AB-VINS to solve pose graph SLAM while only relinearizing a *constant* number of variables, which is proven experimentally.

The rest of the paper is organized as follows: After the complete review of related work in Sec. II, we present in detail the proposed AB-VINS in Sec. III. In Sec. IV AB-VINS is thoroughly evaluated for accuracy, efficiency, and robustness. Finally, in Sec. V, closing remarks are made.

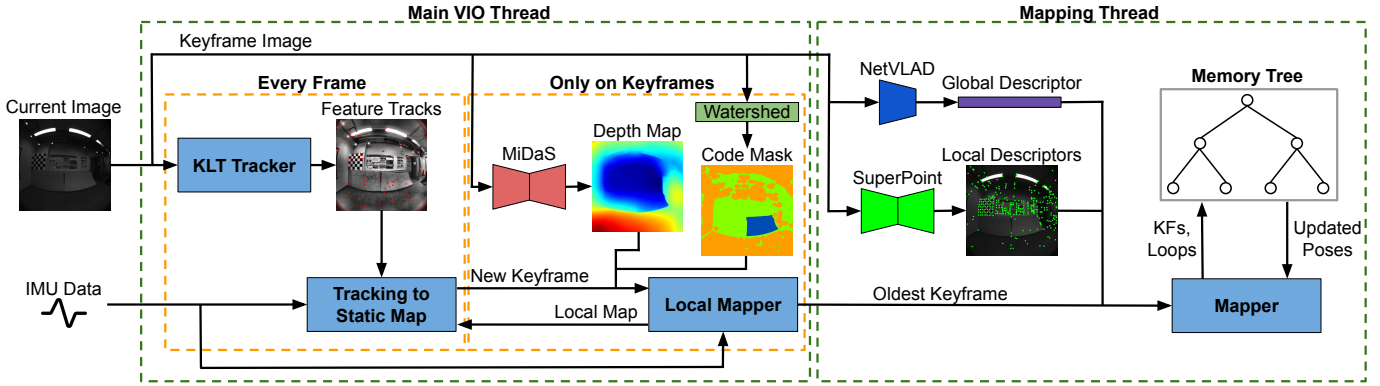


Fig. 2: The proposed AB-VINS system.

II. RELATED WORK

The proposed AB-VINS is related to both visual-inertial SLAM and dense SLAM systems. Because of the introduction of the memory tree, AB-VINS is also related to efficient pose graph optimization methods.

A. Visual-Inertial SLAM Systems

A multitude of visual-inertial SLAM systems have been presented in recent years. The most similar one in nature to AB-VINS is VI-ORB-SLAM [1], which is incorporated into ORB-SLAM3 [2]. Similar to AB-VINS, VI-ORB-SLAM has three modules: tracking, local mapping, and mapping. Just like AB-VINS, it is an optimization-based system, but despite using one more CPU thread than AB-VINS, it does not provide dense depth. In fact, none of the systems mentioned in this section provide dense depth. VINS-Mono [3], later called VINS-Fusion, similarly to AB-VINS has two threads – one for visual-inertial odometry (VIO) and one for mapping. Another visual-inertial SLAM system, ROVIOLI [4], similarly has a VIO front-end and pose graph back-end, and supports multi-session mapping and localization. BASALT [5] attempts to solve the problem of degraded IMU information for keyframes, and solves loop closures in a global bundle adjustment (BA), which may be computationally expensive. OKVIS2 [6] is a recent visual-inertial SLAM system which utilizes a semantic segmentation network to ignore features that should not be tracked (such as on clouds). The main drawback of all of these methods is that the number of variables affected by the global optimization grows linearly with the number of keyframes, while AB-VINS can solve loop closures while only relinearizing a *constant* number of variables.

Unlike visual-inertial SLAM systems, pure visual-inertial odometry (VIO) methods do not have a memory about places, and thus the system steadily drifts over time – but is highly accurate locally. Many VIO systems have been proposed. The multi-state constraint Kalman filter (MSCKF) [7] is one of the first examples of a pure VIO system. MSCKF avoids estimating the structure in the extended Kalman filter (EKF) framework, which can be expensive with more than just a few features, by applying a nullspace projection trick to eliminate the dependency on the feature states. MSCKF has been

adapted and improved many times by adding small amounts of structure to the state [8], adding online calibration and improving consistency [9], and utilizing the efficient sparse square root inverse covariance EKF form [10]. Robocentric VIO (R-VIO) [11], which is also based on the EKF, showed that estimating the poses in a local robocentric frame (the oldest frame in the sliding window) rather than in the global as usual has better observability properties. R-VIO partially inspired the anchored local mapping window of AB-VINS (discussed in Sec. III-C3), however instead of defining the anchored frame in the last frame of the sliding window, we define it in the gravity-aligned frame centered at the oldest frame in the window so that the local gravity direction does not have to be estimated. Another popular type of VIO system is based on nonlinear optimization. A popular method is to marginalize states that are removed from the optimization in order to maintain a large covariance matrix for additional prior cost terms [3, 5, 6, 12]. However, the computational cost of marginalization is high in optimization-based systems compared to EKF-based systems due to the cost of calculating the marginal covariance, which is the main reason we choose to omit marginalization in AB-VINS and instead opt to simply fix the oldest pose in the sliding window similarly to ORB-SLAM.

B. Dense SLAM Systems

Dense VINS systems provide both high-rate gravity-aligned poses and dense depth. Kimera [13] provides dense depth via Delaunay triangulation on the sparse VIO points, however this is an oversimplification of the scene and can not capture small details of the structure. CodeVIO [14] is a dense VIO system which, similarly to AB-VINS, estimates correction terms for the depth within the state, but the correction terms (codes) are learned from an autoencoder network. The codes in AB-VINS are more hand-crafted, but can more easily push or pull entire objects with only a few feature measurements. DiT-SLAM [15] showed that the code dimension can be as low as 8. In AB-VINS on the other hand, the code dimension is 4. SimpleMapping [16] utilizes a deep multi-view stereo (MVS) network to provide dense depth, but does not utilize monocular priors to help the system when parallax is not available.

Purely visual dense SLAM systems have also been proposed. The scale can not be estimated using only classical methods for monocular visual SLAM. DTAM [17] is the first example of such a system, which estimates the pose via dense image alignment, and creates dense depth maps with classical MVS. TANDEM [18], which pairs an MVS network with monocular visual odometry, and receives localization measurements from the TSDF map it maintains from fusing the dense depth. Some visual SLAM systems, like CNN-SLAM [19], BA-Net [20], CodeSLAM [21], and Deep Factors [22] can estimate metric scale by training a monocular depth network with metric depth supervision. However, training a network in such a way does not benefit from the robustness that eliminating the scale and bias from monocular depth as in MiDaS [23] provides. AB-VINS can estimate metric scale because of the IMU, and still benefits from the robustness of MiDaS.

C. Efficient Pose Graph Optimization Methods

One of the first efficient solutions to pose graph optimization is sparse pose adjustment (SPA) [24], which utilizes the sparse information matrix structure in a Levenberg–Marquardt optimization to its advantage. Another option is to utilize the square-root information form as in iSAM [25] and iSAM2 [26]. iSAM2 introduced a data structure called the Bayes tree, which is used to reduce the number of times variables need to be relinearized by using the tree to identify which parts of the graph are affected by the measurements – making optimization highly-efficient. The proposed memory tree is not related to the Bayes tree since the keyframe poses are defined in a relative frame rather than the global. SPA, iSAM, and iSAM2, as well as most other factor graph optimizations ever proposed, define all of the poses in the global frame, which requires at least adjusting all of the poses in-between two loop keyframes. Most similar to the proposed memory tree data structure is the relative method [27], where a keyframe’s pose is defined relative to the previous one’s frame of reference. While the relative method [27] was only applied to an incremental BA and not pose graphs, it could theoretically be used for pose graphs as well – just like the memory tree could be applied to an incremental BA. Just like the memory tree, the relative method allows for the majority of the poses to be fixed, however the proposed memory tree has better algorithmic properties such as theoretically smaller maximum state size and time to compute the global pose as well as optimization with better worst-case complexity.

III. AB-VINS

In this section, the proposed AB-VINS system is detailed in full. A diagram of AB-VINS can be seen in Fig. 2.

A. Initialization

While some recent methods have utilized monocular depth to improve visual-inertial initialization [28, 29], those initialization procedures still wait some time to initialize, and require at least a small amount of motion. In AB-VINS, we adopt a

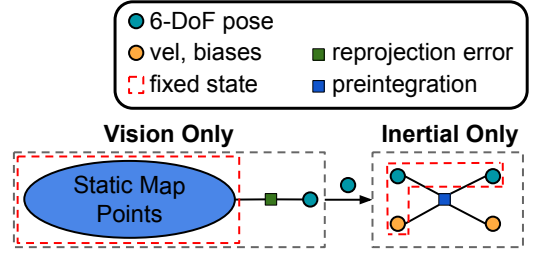


Fig. 3: A graphical representation of tracking to static map. The 6-DoF pose is estimated from the static map using only visual measurements, and an inertial-only optimization estimates the velocity and biases.

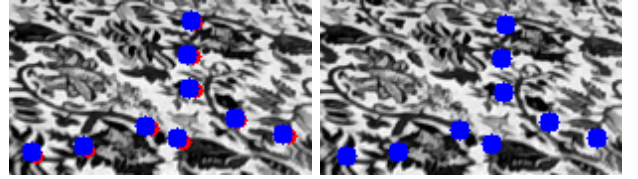


Fig. 4: **Left:** The result of tightly coupling the visual and inertial measurements in the tracking optimization. **Right:** The result of the proposed decoupled approach. Tracked image coordinates are in red and reprojected points are in blue.

much simpler initializer. We assume that the IMU biases are known well enough to integrate, which can easily be obtained offline by letting the device sit still. We first estimate the gravity direction by running Gram–Schmidt on the first few accelerometer measurements. While this does make a static assumption, we found that it works well except in the most dynamic scenarios, which may not be typical for AR/VR headsets or many robotics applications (e.g., wheeled robots or MAV inspection) anyway. Then, we initialize the gravity-aligned map with the first frame’s monocular depth using an arbitrary scale a_0, b_0 . Finally, the velocity is set to zero, and tracking to the static map commences. Thus, we can typically initialize using just the first frame. No motion is required to initialize, but some excitation is needed to estimate the scale. However, we argue that with very little motion (sitting mostly or completely still) scale is not as important as it is with large motions.

B. Tracking to Static Map

For an incoming frame at time t_k , feature tracks are first obtained using the efficient Kenade-Lucas-Tomasi (KLT) tracking algorithm [30] on FAST corner points [31]. Then, the current pose is predicted from preintegrated measurements between the last frame and the current. After that, tracking to the static local map occurs. We track 123 feature points by default.

A visualization of tracking to a static map can be seen in Fig. 3. First the 6-DoF pose, represented as a JPL quaternion [32] ${}^A_k \bar{q}$ and 3D position vector ${}^A \mathbf{p}_{I_k}$, are estimated with only visual measurements – reprojecting points from the static

local map¹. $\{A\}$ is the gravity-aligned anchor frame of the local mapping window (discussed in the next section), and $\{I_k\}$ is the IMU frame at time t_k . Formally, the vision-only optimization attempts to minimize a cost function \mathcal{C}_{vo} defined as

$$\mathcal{C}_{vo} = \sum_{\ell \in \mathcal{V}_k} \lambda_\ell \rho_c (\|\mathbf{r}_{\ell k}^{rs}\|_{\Sigma_v}^2) \quad (1)$$

where \mathcal{V}_k is the index set of all 3D points ${}^A\mathbf{p}_{f_\ell}$ visible in the current frame, λ_ℓ is the edge weight proposed by [29], which down-weights the cost for residuals corresponding to depth points that are near the image edge or have a high depth edge value. The edge images correspond to the depth map that the 3D point ${}^A\mathbf{p}_{f_\ell}$ originates from. The function ρ_c is the robust Cauchy loss function, Σ_v is the diagonal noise covariance matrix for the residual (set to identity in our implementation), and the residual $\mathbf{r}_{\ell k}^{rs}$ is defined as

$$\mathbf{r}_{\ell k}^{rs} = \mathbf{u}_{\ell k} - h_{rs}({}_A^I \hat{q}, {}^A \hat{\mathbf{p}}_{I_k}, {}^A \mathbf{p}_{f_\ell}, {}^C_I \bar{q}, {}^C \mathbf{p}_I, \zeta) \quad (2)$$

where h_{rs} projects the point ${}^A\mathbf{p}_{f_\ell}$ into the current frame using the current pose estimate, $\mathbf{u}_{\ell k}$ is the raw pixel coordinate of the current feature track location for the ℓ th 3D point, and ${}^C_I \bar{q}, {}^C \mathbf{p}_I, \zeta$ are the camera extrinsic and intrinsic calibration parameters from the local mapper. Note that the 3D point and calibration are fixed for this optimization. The optimization is run up to four times, and after each step each residual is run through a χ^2 check. If the residual fails the χ^2 check, it is removed from the next round of optimization. At most 50% of residuals can be removed this way. This process robustifies against bad feature tracks or noisy 3D points.

After the vision-only optimization, the velocity ${}^A\mathbf{v}_{I_k}$ and IMU biases $\mathbf{b}_{g,k}, \mathbf{b}_{a,k}$ are estimated in an inertial-only optimization (only preintegration measurements) with poses of the previous keyframe and current frame fixed. For the preintegration, the angular velocity is integrated using the quaternion integrator [32] and the acceleration is double integrated using fourth order Runge-Kutta. In the case where the IMU measurements (angular velocity or linear acceleration) exceed a saturation threshold, the corresponding measurement noise is inflated to robustify the system against IMU saturation. In particular, the inertial-only optimization tries to minimize the cost function \mathcal{C}_{io} where

$$\mathcal{C}_{io} = \|\hat{\mathbf{x}}_k \boxminus h_p(\mathbf{x}_i, {}^i\boldsymbol{\alpha}_k, {}^i\boldsymbol{\beta}_k)\|_{\mathbf{Q}_{ik}}^2 \quad (3)$$

is the preintegration [33, 34, 35] cost function between the previous keyframe at time t_i and the current frame at time t_k .

We have the state $\hat{\mathbf{x}}_k = \begin{bmatrix} I_k \bar{q}^\top & A \mathbf{p}_{I_k}^\top & A \hat{\mathbf{v}}_{I_k}^\top & \hat{\mathbf{b}}_{g,k}^\top & \hat{\mathbf{b}}_{a,k}^\top \end{bmatrix}^\top$ which is an inertial state (note that the pose is fixed), and similarly for the completely fixed keyframe state \mathbf{x}_i . The terms

¹Note that since the local map is scaled and gravity-aligned, the pose output of the vision-only optimization is scaled and gravity-aligned since it is equivalent to the perspective n point (PnP) problem with a good initial guess from the IMU.

${}^i\boldsymbol{\alpha}_k$ and ${}^i\boldsymbol{\beta}_k$ are the preintegrated measurements between t_i and t_k defined as

$$\begin{aligned} {}^i\boldsymbol{\alpha}_k &= \int_{t_i}^{t_k} \int_{t_i}^s {}^i_u \Delta \mathbf{R} (\mathbf{a}_m(u) - \mathbf{b}_a(u) - \mathbf{n}_a(u)) du ds \\ {}^i\boldsymbol{\beta}_k &= \int_{t_i}^{t_k} {}^i_u \Delta \mathbf{R} (\mathbf{a}_m(u) - \mathbf{b}_a(u) - \mathbf{n}_a(u)) du. \end{aligned} \quad (4)$$

\mathbf{Q}_{ik} is the covariance matrix for the preintegration residual, which can be inflated as discussed if there is IMU saturation detected.

In AB-VINS, we choose a tracking optimization that decouples the visual and inertial measurements. This is because we found that tightly coupling the visual and inertial measurements in the tracking optimization (e.g., as in [1]) can sometimes pull the solution away from one that satisfies the reprojection error, as seen in Fig. 4, which creates wobblier pose output than desired for many applications. The problem is exacerbated when tracking a small number of features as in our system – since the vision terms can not outweigh the inertial – and the noisiness of the monocular depth does not help either. We emphasize that our decoupled approach is only possible with nonlinear optimization and not with a filter, as filters naturally tightly couple the measurements by using inertial measurements for propagation and visual ones for update – which adds priors from both measurements to the pose states.

C. Local Mapping

Every so often the current frame is selected to be a keyframe. A new keyframe is made when the percent of features visible in the current frame compared to the most recent keyframe falls below a threshold. Thus if the camera is always looking at the same thing, no new keyframe will be made. Keyframes are pushed onto a local mapping window, but first a monocular depth network (MiDaS [23, 36]) is run on the raw image² to obtain an affine-invariant inverse depth map which is up to a scale and bias parameter a and b , respectively. The scale and bias, a and b , as well as some other terms to correct the depth are estimated in the place of each feature position separately, which we call the AB feature representation.

1) *AB Features*: Given a and b , and an affine-invariant inverse depth prediction d_{inv} normalized into the $[0, 1]$ range, we have $z_{inv} = ad_{inv} + b$, where z_{inv} is the metric inverse depth. To estimate a and b in a nonlinear optimization, we represent them as s and t , where

$$a = a_{min} + (a_{max} - a_{min})\text{sigmoid}(s) \quad (5)$$

$$b = b_{min} + (b_{max} - b_{min})\text{sigmoid}(t). \quad (6)$$

This makes it so that the scene scale can not become too large or too small in low-excitation scenarios, when scale is unobservable. We use the DPT [36] Swin2 [37] tiny transformer model open-sourced by MiDaS, which is applicable to embedded devices.

²All networks are run on the raw instead of rectified image in order to benefit from the full available FoV.

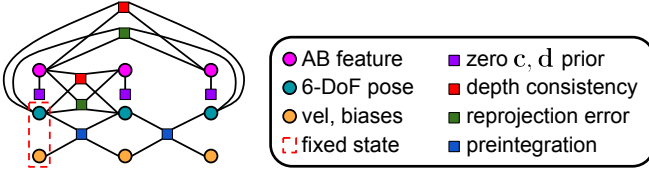


Fig. 5: A graphical representation of the local mapping optimization with three keyframes. For concise presentation, calibration states are not shown.

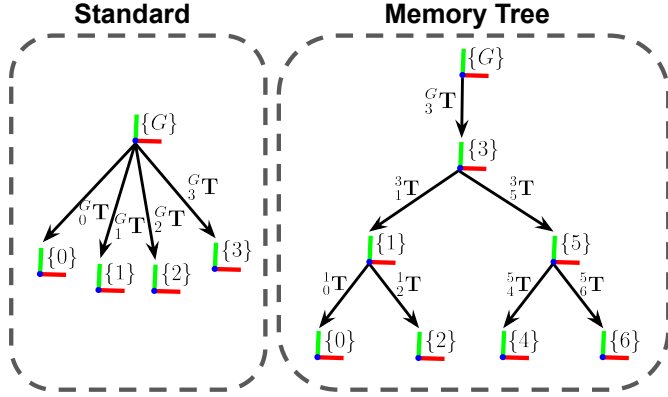


Fig. 6: A comparison of the pose definitions in standard factor graphs (left) and our memory tree (right). In the memory tree, poses are defined in the parent frame for nodes within a binary search tree rather than all in one global frame.

The watershed algorithm is then used on the edge image to create what we call a code mask, which partitions the image into C different regions. Using the code mask, for each keyframe a C -dimensional code vector \mathbf{c} is estimated to push and pull different regions of the depth map in order to correct it using multi-view information. Given a code mask element m for d_{inv} we can write

$$z_{inv} = a(d_{inv} + c[m]) + b \quad (7)$$

where $x[i]$ indexes a vector \mathbf{x} . C in our system is 4.

After \mathbf{c} of course comes \mathbf{d} . We estimate a 4-dimensional vector \mathbf{d} in order to make up for the fact that we use normalized bearings in AB-VINS, and run the MiDaS network on raw distorted images, while it was trained on a simple pinhole model (because the network predicts inverse depths that are too large near the edge of fisheye images). For \mathbf{d} we write

$$\begin{aligned} r &= \|\mathbf{u}_n\| & \theta &= \text{atan2}(r, 1) \\ \theta_d &= \theta(1 + d[0]\theta^2 + d[1]\theta^4 + d[2]\theta^6 + d[3]\theta^8) & d_c &= \theta_d/r \\ z_{inv} &= ad_c(d_{inv} + c[m]) + b \end{aligned} \quad (8)$$

where \mathbf{u}_n is the ideal image coordinate, which is of course a function $\mathbf{u}_n = \Pi^{-1}(\zeta, \mathbf{u})$ of the camera intrinsics ζ and raw image coordinate \mathbf{u} . Thus \mathbf{d} makes the inverse depth smaller closer to the edges of the image. Since Eq. 8 is nearly identical to the Kannala-Brandt [38] fisheye lens distorting equations,

we call the process of *d fisheye monocular depth*. The estimation of a and b , with the optional \mathbf{c} and \mathbf{d} terms, to represent feature positions is called the AB feature representation.

After obtaining z_{inv} we can write

$${}^C\mathbf{p}_f = \frac{[\mathbf{u}_n^\top \ 1]^\top}{z_{inv} \|[\mathbf{u}_n^\top \ 1]^\top\|} \quad (9)$$

where ${}^C\mathbf{p}_f$ is the feature position in the camera frame. The bearing $[\mathbf{u}_n^\top \ 1]^\top$ has to be normalized to deal with largely distorted camera models. Using this formulation, we can estimate positions for *all* features on the image plane with only a few parameters.

2) *Depth Map Registration*: Before being pushed onto the local mapping window, the depth map is registered to the current local map – linearly estimating a and b using the linear system presented in [23] with the sparse points projected from the local map (the same points used in tracking to static map) as the reference metric inverse depths. Note that we wrap the linear registration in a RANSAC loop to improve the robustness. Linear registration is followed by a nonlinear optimization to jointly estimate a , b , \mathbf{c} , and \mathbf{d} while holding the local map fixed – using the same 3D points as in tracking to static map for both linear and nonlinear registration. The main cost in this optimization is the depth consistency cost, which is similar to the depth consistency costs in [14, 21] but defined in the inverse depth space in order for the cost to focus on closer objects rather than farther ones. The \mathbf{c} and \mathbf{d} terms are initialized to zero, and a zero prior is placed on \mathbf{c} and \mathbf{d} in order to prevent the terms from blowing up, which is similar to the zero-code prior in [14, 21]. In particular, the nonlinear depth map registration attempts to minimize the cost function C_{dr} defined as

$$C_{dr} = \sum_{\ell \in \mathcal{V}_k} \lambda_\ell \rho_c \left(\frac{1}{\sigma_d} (r_{\ell k}^{ds})^2 \right) + \|\mathbf{r}_k^p\|_{\Sigma_p}^2 \quad (10)$$

where

$$r_{\ell k}^{ds} = \hat{z}_{inv_{\ell k}} - h_{ds}({}^A\bar{\mathbf{q}}_\ell, {}^A\mathbf{p}_{I_k}, {}^A\mathbf{p}_{f_\ell}, {}^C\bar{\mathbf{q}}_\ell, {}^C\mathbf{p}_I). \quad (11)$$

$\hat{z}_{inv_{\ell k}}$ is the estimated metric inverse depth of the ℓ th feature at time t_k , and h_{ds} projects the 3D point ${}^A\mathbf{p}_\ell$ into frame k and extracts the inverse depth. σ_d is the manually-tuned noise value for the depth consistency residual. We also have the prior residual

$$\mathbf{r}_k^p = \mathbf{0} - [\mathbf{c}_k^\top \ \mathbf{d}_k^\top]^\top \quad (12)$$

which prevents \mathbf{c}_k and \mathbf{d}_k from becoming too large. Σ_p is the manually-tuned diagonal covariance matrix for the zero prior.

3) *Local Mapping Optimization*: After registration, as shown in Fig. 5 we perform a sliding-window optimization in the local mapper, with the oldest pose, velocity, and biases fixed. Online calibration of the camera intrinsics and extrinsics is also performed in this optimization. The default sliding window size of our system is 9.

All of the poses are defined in the anchored $\{A\}$ frame, which is the gravity-aligned frame centered around the oldest keyframe's frame of reference, and is changed after the oldest keyframe is popped from the window. This is similar to the

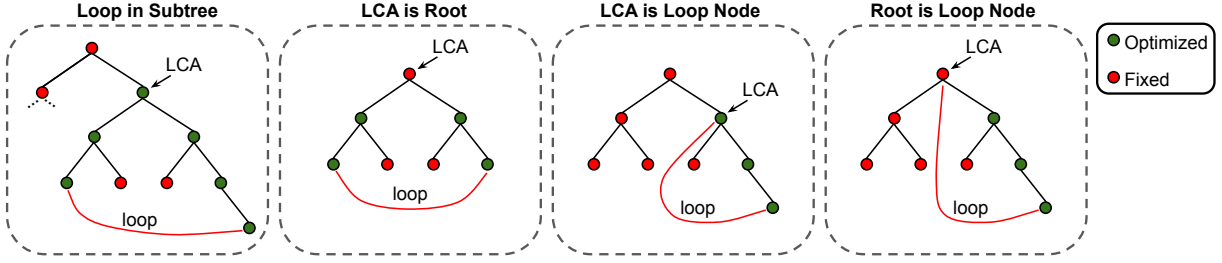


Fig. 7: Examples of different optimization patterns for the memory tree when optimizing the full path between loop nodes.

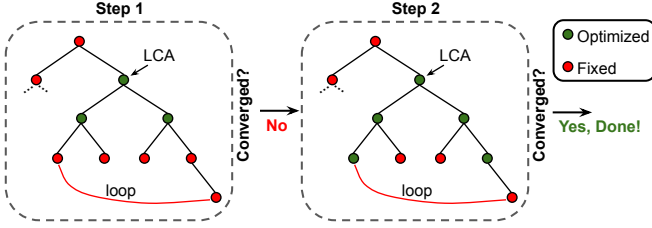


Fig. 8: The process of top-down memory tree optimization. The LCA and its children along the path between the two loop nodes are set variable from the top down until convergence.

robocentric VIO formulation in [11], but [11] defines the robocentric frame to be the oldest frame of reference in the sliding window, which requires actually estimating the gravity direction. On the other hand, our anchored frame is gravity-aligned – only yaw-rotated when the oldest keyframe is popped off the window – and does not required estimating gravity. While the global pose is not tracked in the local mapper, AB-VINS still calculates it for system output by using the most recent global pose in the memory tree to transform poses in the $\{A\}$ frame into the global ³.

Besides the standard reprojection error, our local mapping optimization also includes depth consistency cost. Due to having a dense depth map for each keyframe, every bearing in the sliding window is actually its own landmark, and the landmarks simply have to work together with the oldest landmark via the depth consistency cost to keep the system stable. Once the oldest bearing for a particular feature track is older than the sliding window, it becomes a static 3D landmark ${}^A\mathbf{p}_{f_\ell}$, and replaces the AB feature for the reprojection error and depth consistency. More specifically, the local mapping optimization tries to minimize the cost function \mathcal{C}_{lm} , where

$$\begin{aligned} \mathcal{C}_{lm} = & \sum_{i \in \mathcal{K}} \sum_{\ell \in \mathcal{V}_i^s} \lambda_\ell \rho_c \left(\frac{1}{\sigma_d^2} (r_{\ell i}^{ds})^2 \right) + \sum_{i \in \mathcal{K}} \sum_{\ell \in \mathcal{V}_i^s} \lambda_\ell \rho_c \left(\|\mathbf{r}_{\ell i}^{rs}\|_{\Sigma_v}^2 \right) \\ & + \sum_{i \in \mathcal{K}} \sum_{\ell \in \mathcal{V}_i^v} \lambda_\ell \rho_c \left(\frac{1}{\sigma_d^2} (r_{\ell i}^d)^2 \right) + \sum_{i \in \mathcal{K}} \sum_{\ell \in \mathcal{V}_i^v} \lambda_\ell \rho_c \left(\|\mathbf{r}_{\ell i}^r\|_{\Sigma_v}^2 \right) \\ & + \sum_{i \in \mathcal{K}} \|\hat{\mathbf{x}}_{i+1} \boxminus h_p(\hat{\mathbf{x}}_i, {}^i\boldsymbol{\alpha}_{i+1}, {}^i\boldsymbol{\beta}_{i+1})\|_{\mathbf{Q}_{i,i+1}}^2 + \sum_{i \in \mathcal{K}} \|\mathbf{r}_i^p\|_{\Sigma_p}^2 \end{aligned} \quad (13)$$

³Note that traversal of the memory tree to calculate the global pose, which is logarithmic in the number of keyframes, is done solely in the mapping thread to keep VIO constant-time.

where \mathcal{K} is the index set of all keyframes in the local mapping window, \mathcal{V}_i^s is the index set of all 3D points that are older than the window visible in keyframe i , and \mathcal{V}_i^v is the index set of all 3D points that are not older than the window visible in keyframe i . Note that $\hat{\mathbf{x}}_i$ denotes an inertial state that is completely variable. The residual $r_{\ell i}^d$, which is an extension of $r_{\ell i}^{ds}$ to include two AB features, is defined as

$$r_{\ell i}^d = \hat{z}_{inv\ell a} - h_d \left({}_A^I \hat{q}, {}^A \hat{\mathbf{p}}_{I_k}, \hat{z}_{inv\ell a}, {}_I^C \hat{q}, {}^C \hat{\mathbf{p}}_I, \hat{\boldsymbol{\zeta}}, \mathbf{u}_{\ell a} \right) \quad (14)$$

where $\hat{z}_{inv\ell a}$ is the metric inverse depth in the anchor frame for this 3D point at keyframe index a . Similarly, $\mathbf{r}_{\ell i}^r$ is defined as

$$\mathbf{r}_{\ell i}^r = \mathbf{u}_{\ell i} - h_r \left({}_A^I \hat{q}, {}^A \hat{\mathbf{p}}_{I_k}, \hat{z}_{inv\ell a}, {}_I^C \hat{q}, {}^C \hat{\mathbf{p}}_I, \hat{\boldsymbol{\zeta}}, \mathbf{u}_{\ell a} \right) \quad (15)$$

which projects the 3D point from the inverse depth (parameterized by an AB feature) instead of using an existing static 3D point. The same equation would be valid if we were estimating the inverse depth directly instead of the AB feature, as is standard. Note that the camera extrinsics ${}_I^C \hat{q}$, ${}^C \hat{\mathbf{p}}_I$ and intrinsics $\hat{\boldsymbol{\zeta}}$ are estimated where applicable in the local mapping optimization, including in the residuals $r_{\ell i}^{ds}$ and $\mathbf{r}_{\ell i}^{rs}$. Due to the tight coupling of visual and inertial measurements in this optimization, the local map produced is scaled and gravity-aligned, and due to the sliding-window nature of the optimization, the computation does not grow over time.

D. Mapping with the Memory Tree

After the oldest keyframe is popped off of the local mapping window, it is sent to the mapper, which is responsible for finding and solving for loop closures. As shown in Fig. 2, right before entering the mapper, the keyframe receives a global descriptor from NetVLAD [39] and local descriptors from SuperPoint [40], which are typically different from the FAST corners used by VIO. At this point, in order to save RAM memory, all image-resolution dense matrices (e.g., depth map and code mask) are deleted and only sparse portions are maintained at the local descriptor locations. The global descriptor is PCA compressed to 512 dimensions, and searching for loop candidates with this descriptor is extremely efficient. The local descriptors are used to match local keypoints between loop candidates, and if enough matches are found, Horn's method [41] wrapped in RANSAC is used to compute the relative pose for the pose graph optimization. Upon a loop closure, the loop measurements are sent to the memory tree. The memory tree is a *novel* data structure used to significantly

speed up pose graph optimization. In the following, the details of the memory tree are presented.

1) *Tree Structure*: As seen in Fig. 6, poses in the memory tree are defined in the parent frame within a binary search tree. Only the root’s pose is defined in the global frame. While theoretically, any pose dimension can be used in the memory tree (e.g., 6-DoF SE(3) or 3-DoF SE(2)), since VIO only drifts in 3D position and yaw we adopt the 4-DoF poses

$${}^i_j\mathbf{T} = \begin{bmatrix} \mathbf{R}_z(-{}^j_i\theta_z) & {}^i\mathbf{p}_j \\ \mathbf{0}_{1\times 3} & 1 \end{bmatrix} \quad (16)$$

where ${}^j_i\theta_z$ is the yaw angle, \mathbf{R}_z constructs a yaw-only 3D rotation matrix, and ${}^i\mathbf{p}_j$ is the gravity-aligned position. The keyframe’s timestamp is the search key for the tree. The memory tree is balanced using AVL tree rotation rules [42], which guarantee a perfectly balanced tree no matter what. Since the tree is always balanced, calculating the global pose for any keyframe can be done in $\mathcal{O}(\log(N))$ time if there are N nodes in the tree by repeatedly transforming the pose into the same frame as the parent’s pose until the root node is reached. The benefit of defining the poses in this way is that optimizing a single pose also moves the entire subtree underneath the optimized pose’s node.

To limit the memory usage in areas of repeated visitation, redundant nodes are pruned from the memory tree. A node is considered redundant if a certain percent of the map point visible in it’s keyframe are visible in at least three other frames, which is similar to the keyframe culling criteria of ORB-SLAM [2]. After a node is pruned, the tree is rebalanced, again using the AVL balancing rules, to ensure that the height of the tree is $\mathcal{O}(\log(N))$.

2) *Optimizing the Memory Tree*: Optimizing the memory tree is straightforward. We wish to minimize the cost function \mathcal{C}_{tree} defined as

$$\mathcal{C}_{tree} = \sum_{i \in \mathcal{S}} \rho_c(\|\mathbf{r}_{i,i+1}^{tree}\|_{\Sigma_{tree}}^2) + \sum_{i,j \in \mathcal{L}} \rho_c(\|\mathbf{r}_{ij}^{tree}\|_{\Sigma_{tree}}^2) \quad (17)$$

where \mathcal{S} is the set of necessary sequential connections to add (nodes that are next to each other temporally) and \mathcal{L} is the set of loop connections. Σ_{tree} is the manually-tuned diagonal covariance matrix for tree edges, and ρ_c is again the Cauchy loss function. Given a 4-DoF relative pose measurement ${}^j_i\theta_z$, ${}^i\mathbf{p}_j$ between nodes i and j , the residual is

$$\mathbf{r}_{ij}^{tree} = \begin{bmatrix} {}^j_i\theta_z - ({}^i_L\hat{\theta}_z - {}^j_L\hat{\theta}_z) \\ {}^i\mathbf{p}_j - \mathbf{R}_z({}^i_L\hat{\theta}_z)({}^L\hat{\mathbf{p}}_j - {}^L\hat{\mathbf{p}}_i) \end{bmatrix} \quad (18)$$

where $\{i\}$, $\{j\}$ are the local gravity-aligned frames for nodes i and j , and $\{L\}$ is the gravity-aligned frame centered around the lowest common ancestor (LCA) for nodes i and j . Finding the LCA can be performed in $\mathcal{O}(\log(N))$ time. Of course the poses for the nodes are defined in the parent frame and not the $\{L\}$ frame, but the poses in the $\{L\}$ frame have to be found by transforming iteratively into the same frame as the parent until the $\{L\}$ frame is reached. If optimizing all states in the memory tree, the Hessian structure will be very dense due to correlating more states than usual. Of course, the point of the

memory tree is not to optimize every state, but to carefully choose which states to optimize.

Given two loop candidate tree nodes, we can actually move all the nodes needed to close the loop by only optimizing nodes along the shortest path between the two loop nodes. In order to do this, first the LCA must be found between the two. This is because the shortest path between two loop nodes in the tree always passes through the LCA. To stabilize the optimization, the root node always remains fixed. Note that this does in most cases allow the first ever pose to move, but we argue that the global pose can be simply taken relative to the first pose. Fig. 7 shows different examples of optimization patterns on the memory tree when optimizing the full path between two loop nodes. Note that edges with only fixed parameters need not be included in the optimization. Thus, not all measurements are added to the optimization problem. The path between the two loop nodes is traversed, and only at most $\mathcal{O}(\log(N))$ sequential relative edges are added, and all loop measurements are checked to see if any of their parameters are included in the set of variable parameters. If so, the loop measurement is added, and if not it is left out of the optimization problem.

While optimizing the full path between two loop nodes is already highly efficient, an even more efficient solution exists. Since optimizing a single node’s pose moves the entire subtree underneath, it is possible to start with only optimizing the LCA and its two children, and work our way down until the optimization converges in one iteration. We call this the memory tree top-down optimization algorithm. Fig. 8 shows how this works. This solution is not only highly efficient, but it also solves pose graph SLAM while only relinearizing a *constant* number of variables. This is because on average only three states are variable (the LCA and its two children), while the rest are fixed. However, in the worst case $\mathcal{O}(\log(N))$ states are set variable.

To robustify against potential bad loop closure measurements (e.g., from visual aliasing), we propose a robust yet efficient χ^2 check. Before optimizing the memory tree with a new loop measurement, first the 4-DoF states of all the nodes along the shortest path between the two loop nodes are copied and stored. After optimizing the memory tree, if the new loop residual does not pass a χ^2 test with theoretical threshold γ (i.e., $\|\mathbf{r}_{ij}^{tree}\|_{\Sigma_{tree}}^2 \geq \gamma$ if the newest loop measurement is between nodes i and j), then the old states are copied back into the memory tree to restore it to what it was before, and the loop measurement is discarded. Thus AB-VINS is robust to catastrophically bad loop closures while only using $\mathcal{O}(\log(N))$ extra memory.

3) *Analysis the Memory Tree*: Table I shows the algorithm analysis of different pose graph optimization methods if optimizing with N keyframes. Our memory tree top-down method is the overall best in the table. Looking at the number of variables affected by optimization (i.e., the number of variables that need to be relinearized), the standard method as in SPA [24] and iSAM [25], with the poses defined in the global frame, affects $\Theta(N)$ variables no matter what no matter what. iSAM2 [26] has a chance to affect a constant number of variables under exploration, but typically affects $\mathcal{O}(N)$ variables under a loop closure scenario. The relative method [27]

TABLE I: Algorithm analysis of different pose graph optimization methods with N keyframes.

Method	Num. Variables Affected			Calculate Global Pose			Optimization		
	Best Case	Worst Case	Avg. Case	Best Case	Worst Case	Avg. Case	Best Case	$\mathcal{O}(1)$ Loops	$\mathcal{O}(N)$ Loops
Standard	$\Theta(N)$	$\Theta(N)$	$\Theta(N)$	$\Theta(1)$	$\Theta(1)$	$\Theta(1)$	$\Omega(N)$	$\mathcal{O}(N)$	$\mathcal{O}(N^3)$
iSAM2 [26]	$\Omega(1)$	$\mathcal{O}(N)$	$\mathcal{O}(N)^\dagger$	$\Theta(1)$	$\Theta(1)$	$\Theta(1)$	$\Omega(1)$	$\mathcal{O}(N)$	$\mathcal{O}(N^3)$
Relative [27]	$\Omega(1)$	$\mathcal{O}(N)$	$\Theta(1)$	$\Omega(1)$	$\mathcal{O}(N)$	$\mathcal{O}(N)$	$\Omega(1)^*$	$\mathcal{O}(N^3)$	$\mathcal{O}(N^3)$
Mem. Tree All States	$\Theta(N)$	$\Theta(N)$	$\Theta(N)$	$\Omega(1)$	$\mathcal{O}(\log(N))$	$\mathcal{O}(\log(N))$	$\Theta(N^3)$	$\Theta(N^3)$	$\Theta(N^3)$
Mem. Tree Full Path	$\Omega(1)$	$\mathcal{O}(\log(N))$	$\mathcal{O}(\log(N))^\dagger$	$\Omega(1)$	$\mathcal{O}(\log(N))$	$\mathcal{O}(\log(N))$	$\Omega(1)$	$\mathcal{O}((\log(N))^3)$	$\mathcal{O}(N \log(N))$
Mem. Tree Top-Down	$\Omega(1)$	$\mathcal{O}(\log(N))$	$\mathcal{O}(1)$	$\Omega(1)$	$\mathcal{O}(\log(N))$	$\mathcal{O}(\log(N))$	$\Omega(1)$	$\mathcal{O}((\log(N))^3)$	$\mathcal{O}(N \log(N))$

[†]Assuming a loop-closure scenario. Number of variables affected is constant under exploration.

*Complexity would be $\Omega(N)$ if following the method in the original paper [27] (i.e., including every measurement instead of just the necessary ones).

TABLE II: ATE (deg/m) on the AR Table dataset.

Type	Algorithm	table 1	table 2	table 3	table 4	table 5	table 6	table 7	table 8	Average
VIO	OKVIS [12]	1.769 / 0.096	1.472 / 0.061	3.519 / 0.123	0.919 / 0.139	0.667 / 0.055	1.062 / 0.078	3.373 / 0.166	2.096 / 0.197	1.860 / 0.114
	OpenVINS [43]	1.019 / 0.059	0.984 / 0.032	1.309 / 0.042	0.650 / 0.043	0.914 / 0.032	1.218 / 0.043	1.055 / 0.054	0.965 / 0.084	1.014 / 0.049
	AB-VINS VIO	4.536 / 0.264	1.577 / 0.475	5.318 / 0.553	3.070 / 0.354	5.379 / 0.315	4.033 / 0.380	3.994 / 0.899	5.965 / 0.882	4.234 / 0.515
	AB-VINS VIO no c	9.061 / 0.682	2.053 / 2.434	10.286 / 0.803	7.749 / 0.956	18.582 / 1.705	8.545 / 1.525	4.837 / 1.008	9.833 / 2.719	8.868 / 1.479
	AB-VINS VIO no d	8.465 / 0.853	3.004 / 2.454	11.916 / 1.280	4.996 / 1.059	11.652 / 0.975	7.094 / 1.114	6.741 / 1.163	3.714 / 2.644	7.198 / 1.443
	AB-VINS VIO + Depth Sens.	4.179 / 0.129	1.428 / 0.039	2.011 / 0.165	3.572 / 0.182	1.488 / 0.088	2.410 / 0.098	2.699 / 0.344	5.017 / 0.592	2.850 / 0.205
SLAM	VINS-Fusion [3]	0.631 / 0.042	1.006 / 0.106	0.421 / 0.025	0.658 / 0.043	0.653 / 0.019	0.609 / 0.064	0.814 / 0.036	0.662 / 0.053	0.682 / 0.049
	ORB-SLAM3 [2]	2.385 / 0.079	3.248 / 0.067	2.584 / 0.048	2.601 / 0.116	2.180 / 0.113	1.543 / 0.127	2.065 / 0.187	1.003 / 0.145	2.201 / <u>0.110</u>
	AB-VINS	4.445 / 0.292	3.449 / 0.628	4.816 / 0.417	3.869 / 0.369	6.528 / 0.281	4.712 / 0.389	7.335 / 0.787	3.634 / 0.693	4.849 / 0.482

TABLE III: ATE (deg/m) on the TUM-VI dataset.

Type	Algorithm	room 1	room 2	room 3	room 4	room 5	room 6	Average
VIO	OKVIS	1.007 / 0.050	0.776 / 0.126	1.092 / 0.069	0.959 / 0.039	1.854 / 0.064	0.584 / 0.047	1.045 / 0.066
	OpenVINS	1.263 / 0.058	2.395 / 0.075	1.362 / 0.076	0.845 / 0.041	1.423 / 0.083	0.754 / 0.032	1.340 / 0.061
	AB-VINS VIO	1.987 / 0.508	5.737 / 3.260	6.110 / 1.412	1.347 / 0.190	3.160 / 0.627	1.583 / 0.174	3.321 / 1.028
SLAM	VINS-Fusion	0.760 / 0.046	1.419 / 0.104	0.698 / 0.051	0.567 / 0.026	1.701 / 0.063	0.698 / 0.048	<u>0.974 / 0.057</u>
	ORB-SLAM3	0.482 / 0.012	0.607 / 0.015	1.315 / 0.038	0.481 / 0.014	0.531 / 0.014	0.465 / 0.013	0.647 / 0.018
	AB-VINS	4.615 / 0.311	5.092 / 0.462	4.331 / 0.181	1.714 / 0.112	4.372 / 0.466	1.294 / 0.190	3.570 / 0.287

can affect up to $\mathcal{O}(N)$ variables, but on average can affect only a constant number of variables due to only optimizing the beginning and end of each loop. The memory tree top-down method can also affect a constant number of variables, but in the worst case is only $\mathcal{O}(\log(N))$, and only affects a constant number of variables on average even under loop closure scenarios. Moving on to the global pose calculation, defining the poses in the global frame as is standard allows for constant-time global pose calculation. For the relative method, global pose calculation typically takes $\mathcal{O}(N)$ time since each keyframe pose is defined in the previous one’s frame of reference, and thus the global pose is dependent on each previous keyframe. On the other hand, with the memory tree, global pose calculation is typically done in $\mathcal{O}(\log(N))$ time due to the efficient tree structure of the pose definitions. It should be noted that the computation incurred by having to relinearize a larger number of variables is much higher than having to iterate to find the global pose.

The final analysis presented in Table I is the computational complexity of the overall optimization. Note that an average case is not reported here since the complexity depends on the number of loop measurements, which depends on the environment. Thus, there are two worst cases reported for $\mathcal{O}(1)$ and $\mathcal{O}(N)$ loop measurements. With a standard pose graph optimization method, the complexity is linear in the absolute best case, which is the same as having a constant number of loops. In the worst case with $\mathcal{O}(N)$ loops, the complexity is $\mathcal{O}(N^3)$ [24]. For iSAM2 [26], the optimization

can be constant-time in the best case (under exploration) but other than that shares the same complexity with the standard pose graph optimization. With the relative method, the best case arises when the two loop keyframes are very close to each other in time, and there are a constant number of loops. In this case, the method can be constant time. In the worst case with a constant number of loops, the complexity is cubic. This is because $\mathcal{O}(N)$ states can be set variable even with a single loop, and the states are all correlated leading to a dense Hessian structure. Similarly, the complexity of the relative method is cubic with $\mathcal{O}(N)$ loops. Note that this analysis of the relative method assumes that 1) it is applied to pose graph optimization and 2) only the necessary measurements are included in the optimization instead of all the measurements as proposed in the original paper [27]. If all measurements are included in the optimization then the best case becomes $\Omega(N)$ due to having to iterate through all of the sequential edges.

Moving on to the the memory tree, with all states set variable, the complexity is cubic in every case. This is due of the cost of Levenberg–Marquardt iterations with a nearly dense Hessian structure. For the full path algorithm, the best case is when there are a constant number of loops and the two loop nodes are near the root of the tree. In this case, the complexity is constant. In the worst case with a constant number of loops, the complexity is $\mathcal{O}((\log(N))^3)$, which is sublinear. This is due to the cost of Levenberg–Marquardt iterations with $\mathcal{O}(\log(N))$ states that are all correlated. In the worst case with $\mathcal{O}(N)$ loops, the complexity is $\mathcal{O}(N \log(N))$

due to having to find the LCA for $\mathcal{O}(N)$ loops to see which measurements should be included in the optimization. For the top-down method, the complexity is the same as the full path algorithm since $\mathcal{O}(\log(N))$ states can be variable in the worst case. If only a constant number of states are variable (which is the average case) with a constant number of loops, the complexity is $\mathcal{O}((\log(N))^2)$ due to having to find the LCA for the $\mathcal{O}(\log(N))$ relative edges. While AB-VINS allows for at most $\mathcal{O}(N)$ loop measurements, some systems such as ORB-SLAM3 [2] allow for up to $\mathcal{O}(N^2)$ loops. If this is the case, the worst case for the full path and top-down algorithms becomes $\mathcal{O}(N^2 \log(N))$, which is still better than the cubic complexity of the other methods.

IV. EXPERIMENTAL RESULTS

AB-VINS is implemented in an efficient C++ code base. Ceres solver [44] with single-thread execution is used for all optimizations. Automatic differentiation provided by `ceres::Jet` is used in all factors except for preintegration and the reprojection error from a static point used in tracking to static map, which use analytical Jacobians. Unlike numerical differentiation via finite differences, automatic differentiation does not come with a large computational overhead or loss of accuracy. We found automatic differentiation to be especially useful for developing the memory tree relative pose factor, since the analytical Jacobians for it are quite complicated. A desktop device equipped with an i5-6600K CPU and RTX 2070 Super GPU with 16GB of RAM is used in all experiments.

A. Accuracy

We first evaluate the accuracy of AB-VINS compared to state-of-the-art VIO [12, 43] and visual-inertial SLAM [2, 3] systems. Trajectories are aligned by finding the best 4-DoF transformation between the estimated and ground truth.

1) *Pose Accuracy on the AR Table Dataset:* We first test on the recently released AR table dataset [45]. This dataset has a single monocular camera with radial and tangential distortion. The results are in Table II, where it can be seen that AB-VINS is not as accurate as state-of-the-art VINS systems, either in VIO or SLAM setting. An ablation study is presented in the table where we investigate the impact of fixing each keyframe’s \mathbf{c} and \mathbf{d} in the local mapping window to zero separately. Clearly it is necessary to estimate both \mathbf{c} and \mathbf{d} to correct the monocular depth. We additionally evaluate the impact of utilizing a depth sensor instead of monocular depth, which is reported in the table. Note that a and b are fixed to 1 and 0 when using the depth sensor. There is a clear improvement from using more accurate depth from the depth sensor rather than the monocular depth, which shows that the biggest reason for AB-VINS being less accurate than the other systems is the reliance on monocular depth. Note that the loop-closed result of AB-VINS (using the memory tree) results in slightly improved position accuracy and slightly degraded orientation accuracy on this dataset. This shows that the memory tree did not hurt the accuracy overall in this case.

TABLE IV: Depth accuracy on the AR Table dataset.

	Method	$\delta_1 \uparrow$	$\delta_2 \uparrow$	$\delta_3 \uparrow$	RMSE \downarrow	MAE \downarrow	$\log_{10} \downarrow$
table 1	MiDaS	0.733	0.949	0.991	0.785	0.124	0.072
	AB	0.724	0.954	0.992	0.756	0.129	0.075
table 2	MiDaS	0.184	0.375	0.627	1.231	0.635	0.251
	AB	0.256	0.529	0.761	1.016	0.551	0.204
table 3	MiDaS	0.656	0.918	0.985	0.833	0.173	0.086
	AB	0.615	0.896	0.972	0.786	0.180	0.095
table 4	MiDaS	0.704	0.956	0.989	0.840	0.137	0.077
	AB	0.694	0.951	0.989	0.804	0.135	0.079
table 5	MiDaS	0.555	0.855	0.963	1.033	0.173	0.106
	AB	0.571	0.858	0.958	1.052	0.171	0.105
table 6	MiDaS	0.529	0.826	0.955	1.012	0.220	0.114
	AB	0.532	0.816	0.938	0.992	0.217	0.116
table 7	MiDaS	0.590	0.883	0.973	0.991	0.145	0.098
	AB	0.513	0.841	0.955	1.069	0.147	0.113
table 8	MiDaS	0.231	0.561	0.873	1.394	0.217	0.178
	AB	0.213	0.553	0.878	1.508	0.209	0.179
Average	MiDaS	0.523	0.790	0.920	1.015	0.228	0.123
	AB	0.515	0.800	0.930	0.998	0.217	0.121

2) *Pose Accuracy on the TUM-VI Dataset:* The next dataset tested on is the TUM-VI dataset [46]. We use the left fisheye camera for evaluation. The results are reported in Table III, where it is clear that AB-VINS is again not as accurate as the state-of-the-art. Notice that the accuracy of AB-VINS with loop closure is significantly higher than the VIO result on this dataset. This shows the capability of the memory tree to improve the accuracy over simply running VIO. All hyperparameters of AB-VINS are the same for the TUM-VI dataset as in the AR Table dataset, which shows the generalization capability of our system.

3) *Depth Accuracy:* The depth output of AB-VINS will ideally be accurate enough for downstream applications such as AR and path planning. We evaluate the accuracy of the depth on the AR Table dataset, which comes with ground-truth depth maps from a depth sensor. Table IV reports the results of evaluating the dense depth output of AB-VINS. We compare the base accuracy of the MiDaS DPT Swin2 Tiny model (denoted as “MiDaS” in the table) to the accuracy of the depth after jointly estimating a , b , \mathbf{c} , and \mathbf{d} in our local mapping optimization (denoted as “AB” in the table). The scale and bias for MiDaS are estimated linearly using sparse depths from the local map (i.e., the same points as tracking to static map and depth map registration) using the linear system from the original paper [23] for a fair comparison. From Table IV it is clear that estimating the AB features results in slightly improved depth accuracy – improving all but one of the metrics in the average case. Additionally, the dense depth accuracy of both MiDaS and the AB features is amenable for downstream applications, with a δ_1 accuracy over 0.5 and RMSE around one meter.

4) *Accuracy of the Memory Tree:* To investigate the accuracy of the memory tree, we turn to the standard 2D pose graph datasets⁴. We incrementally optimize the Manhattan World (M10000 and M3500) datasets as well as the Intel and MIT Killian Court datasets to simulate large-scale SLAM

⁴The datasets can be downloaded here <https://lucacarlone.mit.edu/datasets/>

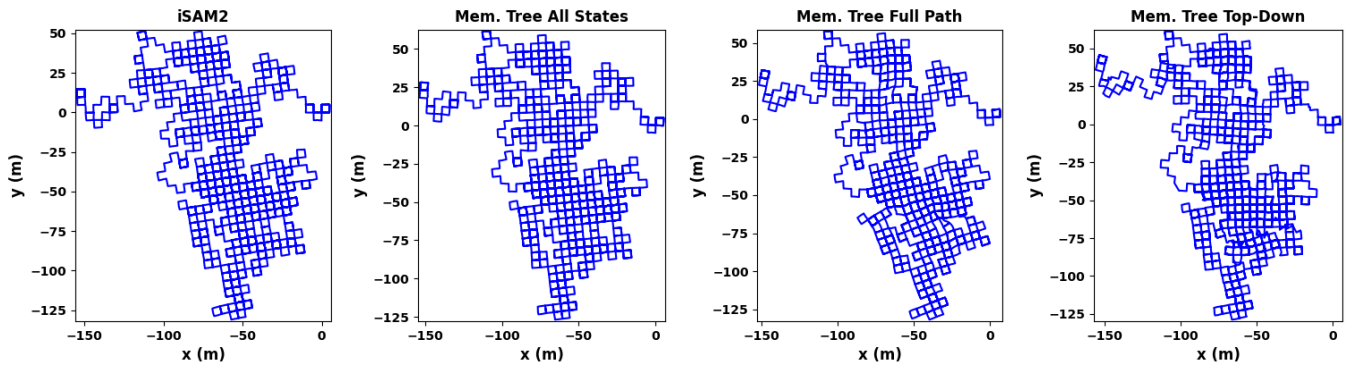


Fig. 9: The trajectory results of different incremental pose graph optimization methods on the M10000 dataset. From left to right: iSAM2 [26], memory tree with all states optimized, memory tree full path, and memory tree top-down.

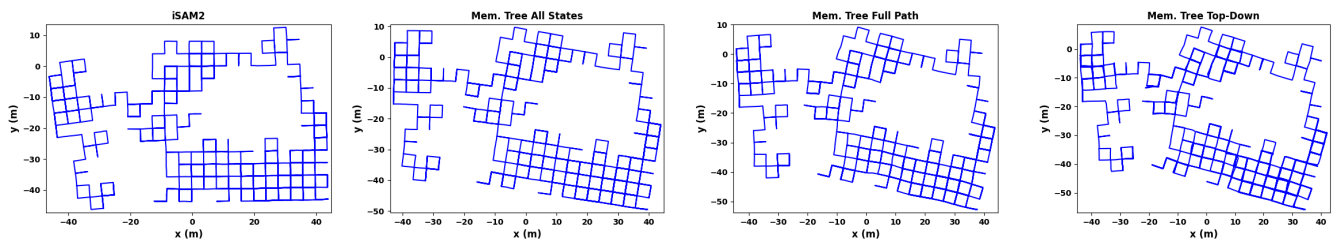


Fig. 10: The trajectory results of different incremental pose graph optimization methods on the M3500 dataset. From left to right: iSAM2 [26], memory tree with all states optimized, memory tree full path, and memory tree top-down.

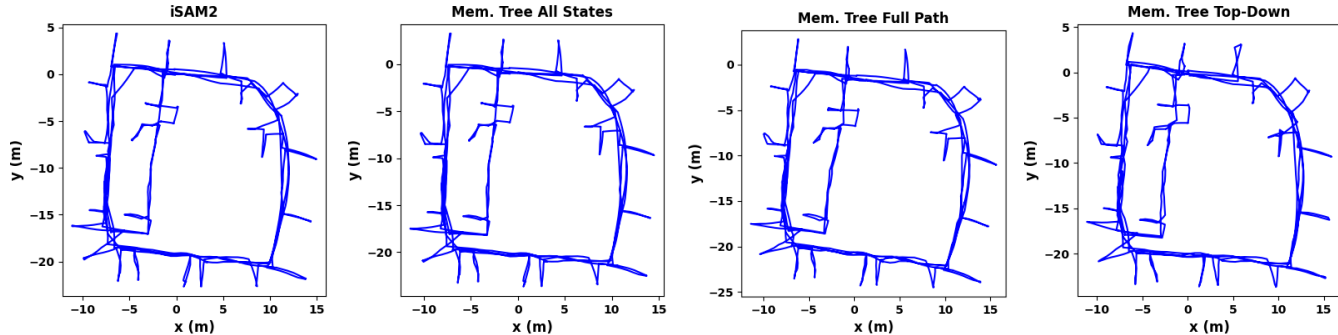


Fig. 11: The trajectory results of different incremental pose graph optimization methods on the Intel dataset. From left to right: iSAM2 [26], memory tree with all states optimized, memory tree full path, and memory tree top-down.

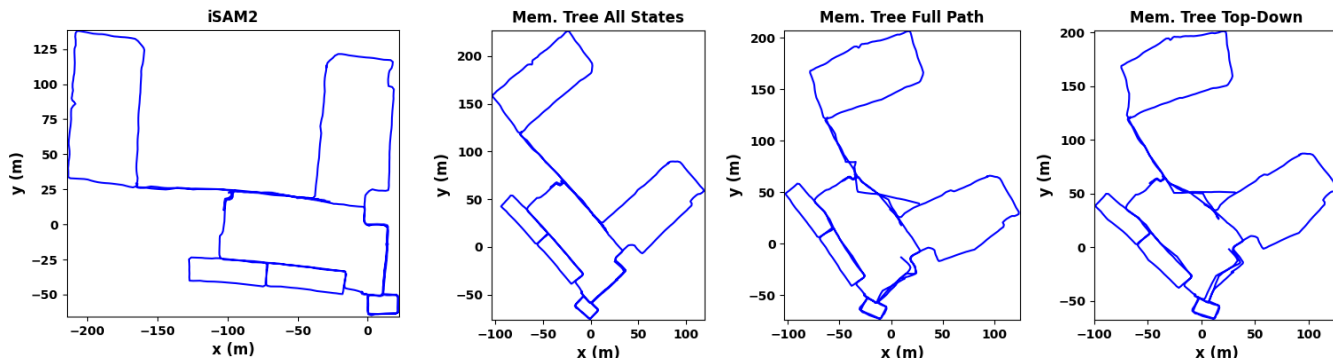


Fig. 12: The trajectory results of different incremental pose graph optimization methods on the MIT Killian Court dataset. From left to right: iSAM2 [26], memory tree with all states optimized, memory tree full path, and memory tree top-down.

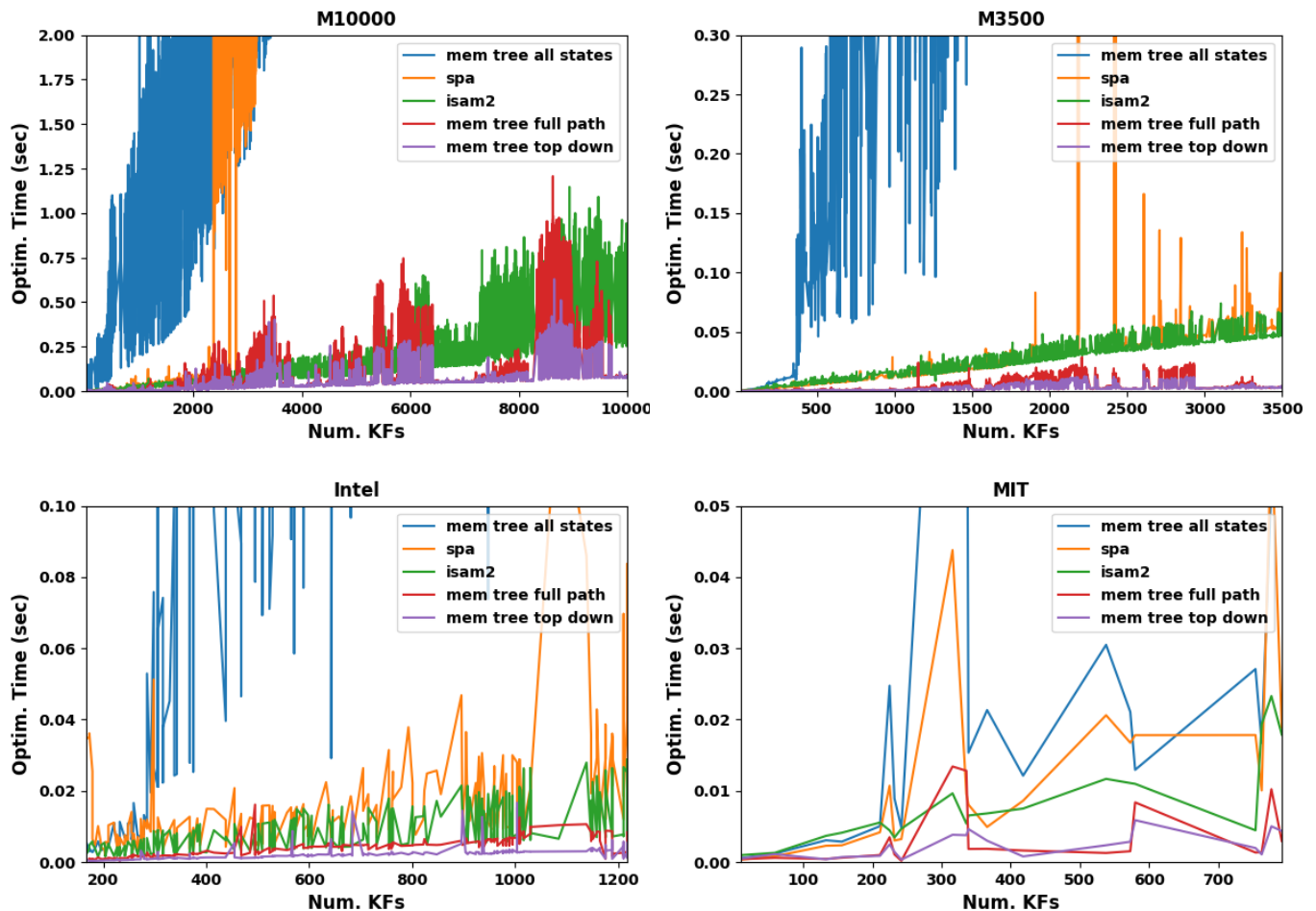


Fig. 13: Timing of different incremental pose graph optimization methods on the different 2D pose graph datasets. Our memory-tree top-down method is by far the most efficient.

settings. Optimization is only carried out when there is a new loop measurement. For the memory tree, which performs 4-DoF pose graph optimization, the z positions are all set to zero in order to utilize the 2D (3-DoF) datasets. Since we only implement 4-DoF (3D position and yaw) pose graph optimization in the memory tree, the 3D (6-DoF) pose graph datasets (e.g., Sphere, Taurus, and Cube) are omitted. We compare to the state-of-the-art incremental pose graph optimization method iSAM2 [26] implemented in GTSAM [47]. We also compare the three methods for optimizing the memory tree: 1) optimizing all states, 2) optimizing the full path between two loop nodes, and 3) the top-down optimization method. The resulting trajectories for the M10000 dataset can be viewed in Fig. 9, the M3500 dataset in Fig. 10, the Intel dataset in Fig. 11, and the MIT dataset in Fig. 12. Note that the memory tree trajectories are typically tilted compared to the iSAM2 trajectory due to the fact that the first frame can not be trivially fixed and has no prior. Again, the global pose output can simply be taken relative to the first ever keyframe in order to match the output of standard methods with the first global pose fixed, but we left the trajectories tilted to show that we do not fix the first pose. Qualitatively it can be seen that optimizing all states in the memory tree results in a trajectory similar to iSAM2, while the other two memory tree methods

are slightly less accurate. Of course in the Manhattan World datasets, a perfect solution would have all of the vertical parts of the trajectory at 90° to the horizontal ones. However, the memory tree full path and top-down methods still produce reasonable results despite optimizing far fewer variables than is typical. On the Intel dataset, there is almost no noticeable degradation in accuracy when using the memory tree full path or top-down method, which shows a case where these methods can nearly match the state-of-the-art solution despite being far more efficient. For the MIT dataset, the performance of these two methods is noticeably worse than iSAM2 and the full batch memory tree solution. While the accuracy is still reasonable for most of the trajectory (e.g., the smaller loops), we believe that the larger loops are less accurate due to the poor odometry accuracy on this dataset. The memory tree full path and top-down methods require highly-accurate odometry in order to produce reasonable results, whereas on the MIT dataset the odometry curves while traversing the long hallways and only optimizing a few states can not correct all of the drift needed.

B. Efficiency

To evaluate efficiency, timing results are reported.

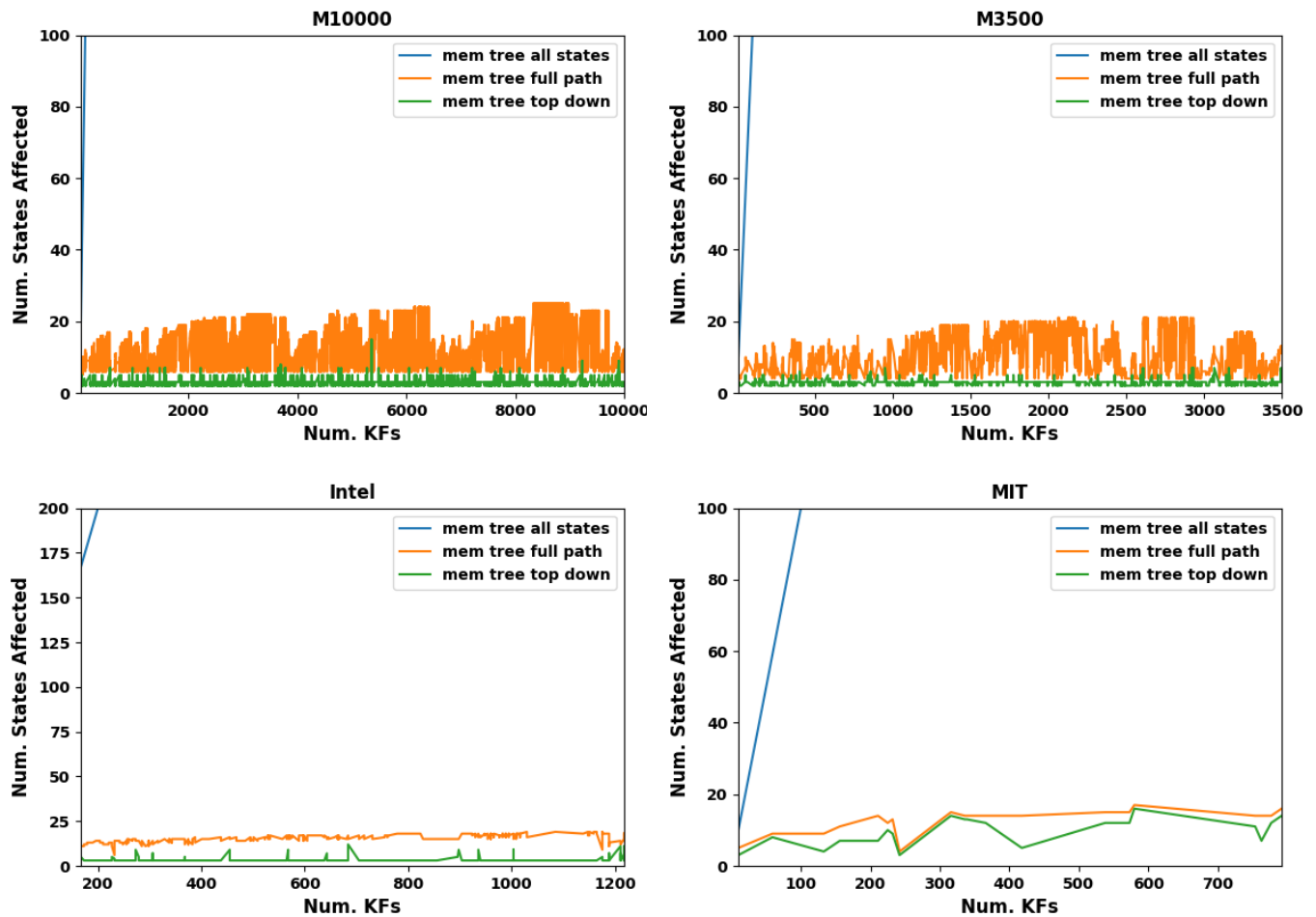


Fig. 14: The number of states affected by optimization over time on the different 2D pose graph datasets. The memory tree top-down method only affects a *constant* number of states on average.

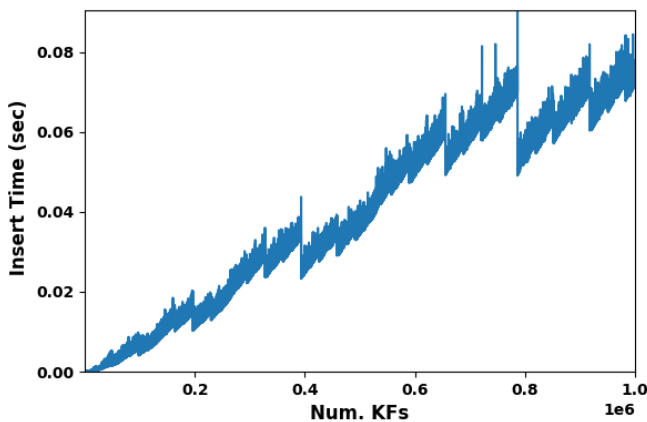


Fig. 15: Timing for inserting the newest node into the memory tree and balancing.

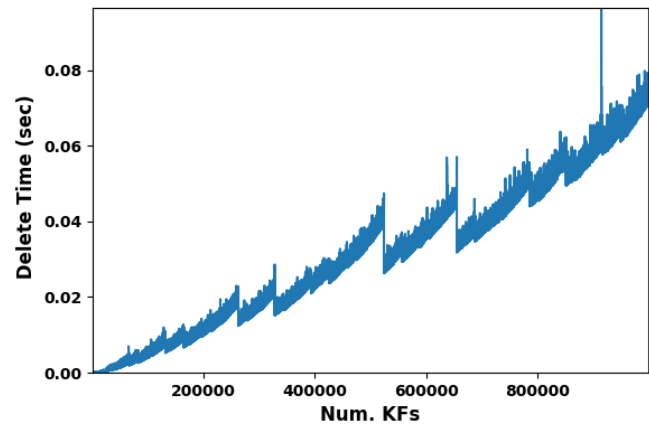


Fig. 16: Timing for deleting the most recent node in the memory tree and balancing.

1) *Efficiency of VIO Thread:* The main VIO thread of ABVINS must be able to keep up with real-time requirements. Luckily, it is highly-efficient. Table V reports the efficiency of different operations of the main VIO thread – namely frame rate operations (feature tracking, vision-only, and inertial-only optimization) as well as keyframe operations (mono depth

inference, depth map registration, and local mapping optimization). The total average time per frame is also reported as 11.5ms. This shows that the main VIO thread can easily keep up with real-time requirements. Note that the total average time per frame reported in Table V includes the keyframe operations (monocular depth inference, depth map registration,

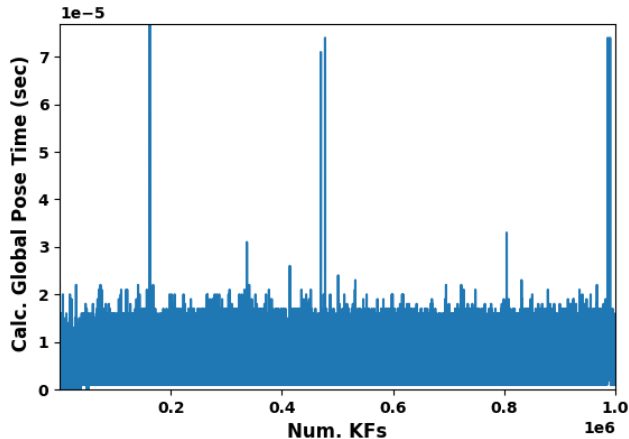


Fig. 17: Timing for calculating the global pose of the newest node in the memory tree. Calculating the global pose never takes more than a handful of microseconds even with one million nodes despite being of logarithmic complexity.

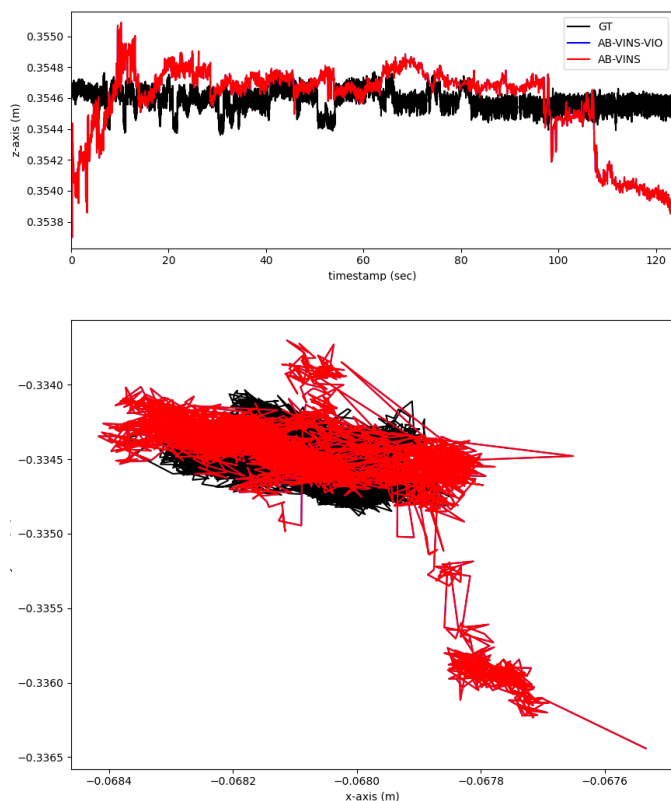


Fig. 18: The trajectory plots from the *static* sequence of the Low/No Excitation dataset. The trajectories for AB-VINS VIO and AB-VINS are equivalent in this sequence and completely overlapping since there is only one keyframe. The trajectories look jagged only because of the extremely small scale of the plots.

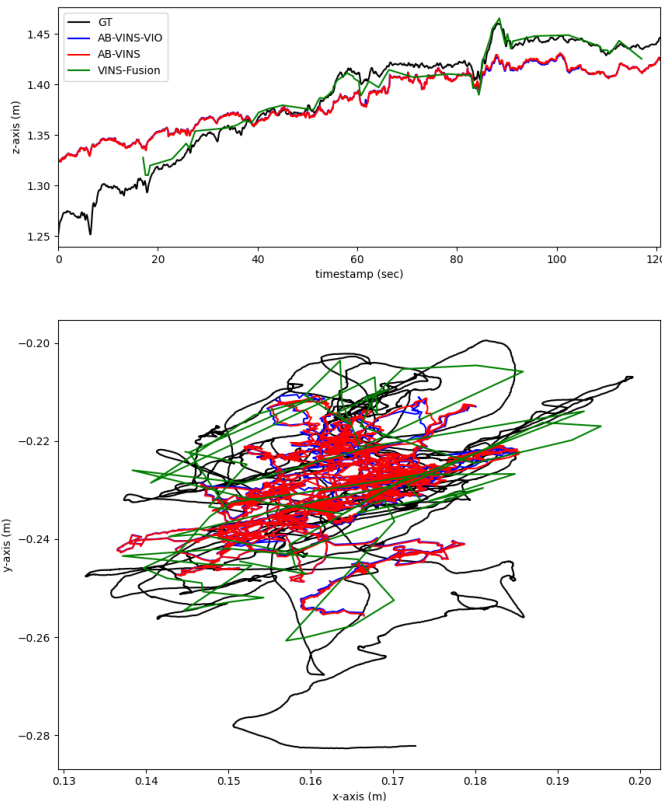


Fig. 19: The trajectory plots from the semi-static sequence of the Low/No Excitation dataset. VINS-Fusion is surprisingly able to initialize on this sequence – probably due to the slight z motion induced by human error of trying to hold the sensors still.

TABLE V: Efficiency of operations in the VIO thread.

Frame Rate Operations		Keyframe Operations	
Operation	Avg. Time (sec)	Operation	Avg. Time (sec)
Feature Tracking	0.0033 ± 0.0018	Mono Depth Inference	0.0173 ± 0.0026
Vision Only	0.0032 ± 0.0016	Depth Map Registration	0.0048 ± 0.0030
Inertial Only	0.0001 ± 0.0002	Local Mapping Opt.	0.0701 ± 0.0345
Total Avg.	0.0115 ± 0.0233		

TABLE VI: Average timing on the AR Table 4 sequence.

Method	Avg. Time (sec)	Estimator	Dense Depth
VINS-Fusion [3]	0.0523 ± 0.0260	Optimization	No
OpenVINS [43]	0.0123 ± 0.0062	EKF	No
AB-VINS	0.0115 ± 0.0233	Optimization	Yes

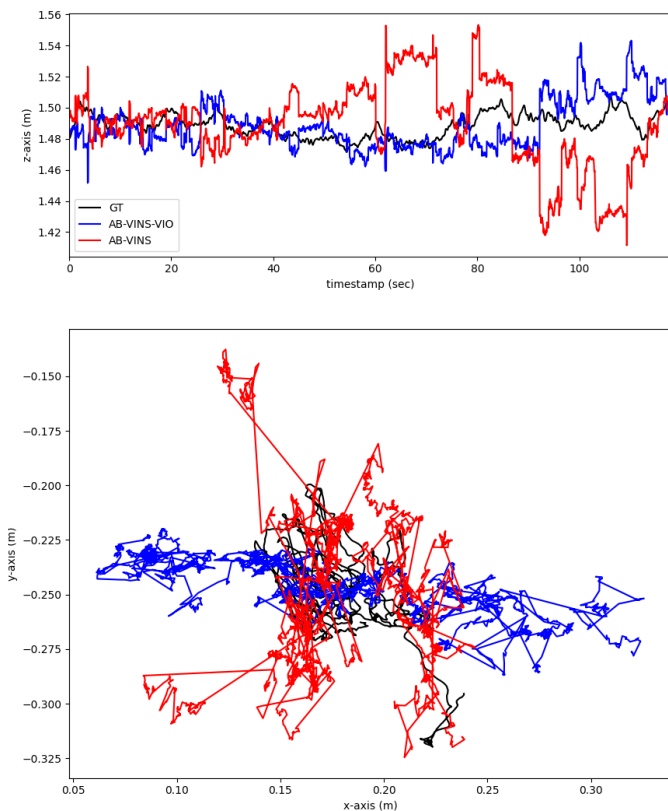


Fig. 20: The trajectory plots from the `rotation` sequence of the Low/No Excitation dataset. Only AB-VINS is able to initialize on this challenging sequence.

and local mapping optimization) in the average.

AB-VINS VIO is also efficient compared to the VIO of other state-of-the-art systems. Table VI shows the comparison. Only methods that use a single VIO thread are reported in the table, which is why ORB-SLAM3 and OKVIS are excluded. VINS-Fusion’s VIO is run in single-thread mode here to obtain the comparison. AB-VINS is much more efficient than a state-of-the-art optimization-based VINS-Fusion, and even surpasses the efficiency of a state-of-the-art filter-based OpenVINS on average while also providing dense depth. Note that launching a separate thread for local mapping as in ORB-SLAM3 would further improve the efficiency of the main thread, since only feature tracking, vision only, and inertial only would be performed on it.

2) *Efficiency of the Memory Tree*: Where the full path and top-down memory tree methods lack in accuracy, they make up for in efficiency. Timing results can be viewed in Fig. 13 for incrementally optimizing on the 2D pose graph datasets. Here we also compare to SPA [24] for reference, which is reimplemented with Ceres solver using automatic differentiation for a fair comparison to our memory tree. SPA was omitted in the accuracy evaluation since the SPA trajectories were very similar to the iSAM2 ones. Note that SPA and iSAM2 have a slight advantage here since the implementation we use is purely 2D (3-DoF) instead of 4-DoF like ours. Optimizing all states of the memory tree is very

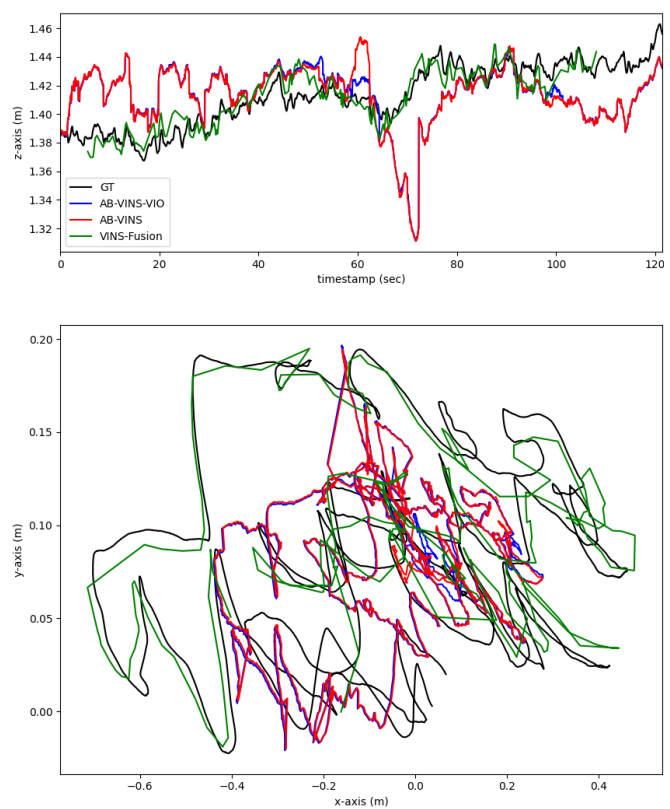


Fig. 21: The trajectory plots from the `motion 1` sequence of the Low/No Excitation dataset. VINS-Fusion is the only fully hand-crafted system to initialize here.

slow – typically slower than SPA – due to the extremely large and dense Hessian structure. Both the full path and top-down methods are more efficient than SPA and iSAM2. Besides the timing, it is also interesting to look at the state size of the optimization. We claim that the top-down optimization solve pose graph SLAM while only adjusting a constant number of variables, and this is proven experimentally in Fig. 14.

We also provide timing for inserting a node into the memory tree – the newest node as is done within AB-VINS – and balancing. This result can be viewed in Fig. 15 for up to one million nodes. Note that nearly all of the computation burden for memory tree insertion is because of the balancing, which is logarithmic with AVL trees but with a high constant overhead due to the cost of rotating the nodes on the way out of the recursive calls to the insert function. The timing for deleting the most recent node from the memory tree can be seen in Fig. 16, where again most of the computational cost comes from balancing. Finally, the cost of calculating the global pose for the most recent node in the memory tree can be seen in Fig. 17. Even though calculating the global pose is logarithmic just like the complexity of balancing, the cost is far lower due to a much smaller number of floating point operations being performed, and only takes a few *microseconds* even with one million nodes in the tree. This validates our design choice for the memory tree, since the global pose, which is needed for downstream applications, can be calculated very efficiently –

TABLE VII: Position ATE (m) on the Low/No Excitation dataset.

Type	Algorithm	static	semi-static	rotation	motion 1	motion 2	motion 3	Average
VIO	OKVIS [12]	-	-	-	-	-	-	- [†]
	OpenVINS [43]	-	-	-	-	0.044	0.109	0.077*
	AB-VINS VIO	0.001	0.029	0.057	0.123	0.099	0.357	<u>0.111</u>
SLAM	VINS-Fusion [3]	-	0.008	-	0.022	0.040	0.069	0.035*
	ORB-SLAM3 [2]	-	-	-	-	-	-	- [†]
	AB-VINS	0.001	0.029	0.051	0.124	0.104	0.287	0.099

[†]Failed to initialize on all sequences so average could not be obtained.

*Failed to initialize on at least one sequence so not considered to be bolded or underlined.

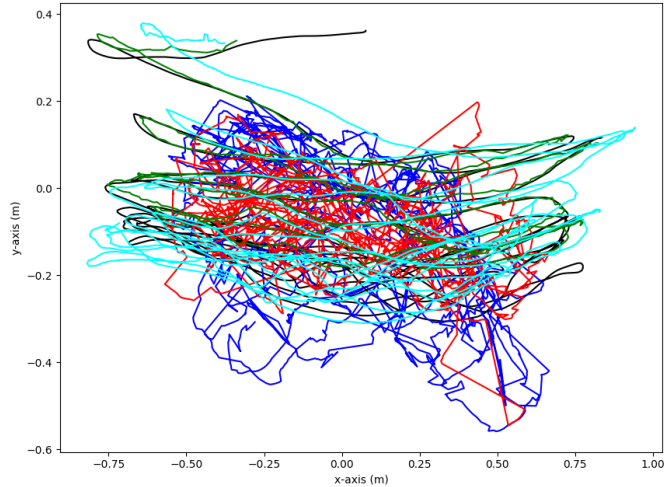
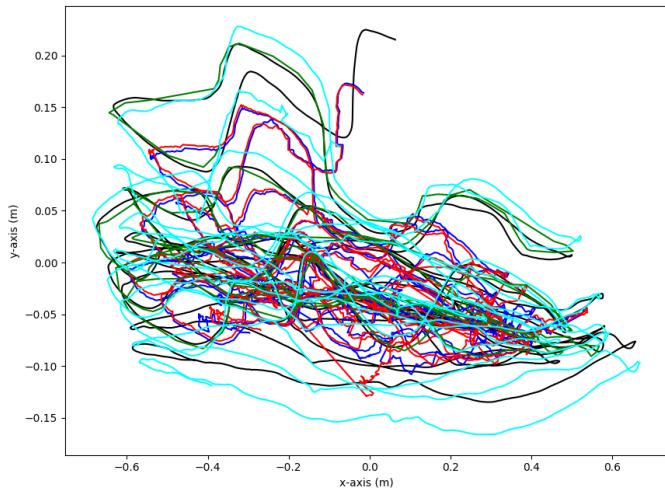
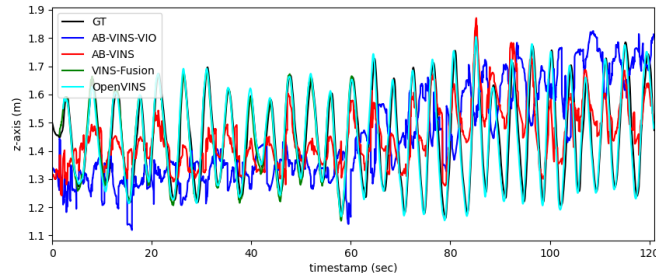
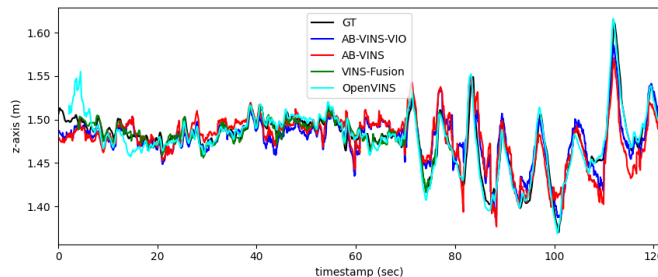


Fig. 22: The trajectory plots from the `motion 2` sequence of the Low/No Excitation dataset. OpenVINS is able to now initialize with this amount of motion.

Fig. 23: The trajectory plots from the `motion 3` sequence of the Low/No Excitation dataset. Despite there being more than a reasonable amount of motion for a typical AR/VR scenario, neither OKVIS or ORB-SLAM3 are able to initialize.

not taking much longer than having the pose defined in the global frame in the first place.

C. Robustness

We have also carefully validated the robustness of the proposed AB-VINS in different challenging scenarios.

1) *Robustness to Degenerate Motions*: It is well-known that completely hand-crafted monocular VINS systems require parallax from sufficient motion to estimate the structure and poses. On the other hand, since AB-VINS estimates the structure using monocular depth, it can work even with absolutely *no motion at all*. To showcase this capability, we collected the Low/No Excitation dataset. The dataset has six different motion profiles. The first is *static*, where the

device sits completely still on a table. The second is called *semi-static*, where the device is held as still as possible in the hand. After that, there is a sequence of rotation-only motion called *rotation*. Finally, there are three levels of motion ranging from 1 to 3. For *motion 1*, the device moves very slowly from side to side, and by *motion 3* the side-to-side motion is more aggressive and includes up-and-down motion as well as rotations. All of the sequences are confined to a small area mostly facing the same thing in order to simulate a typical AR/VR scenario or low-motion robot activity (e.g., an autonomous vehicle sitting still at a traffic light or a drone hovering). The same sensor rig as the AR Table dataset is used. The results are reported in Table VII. Note that

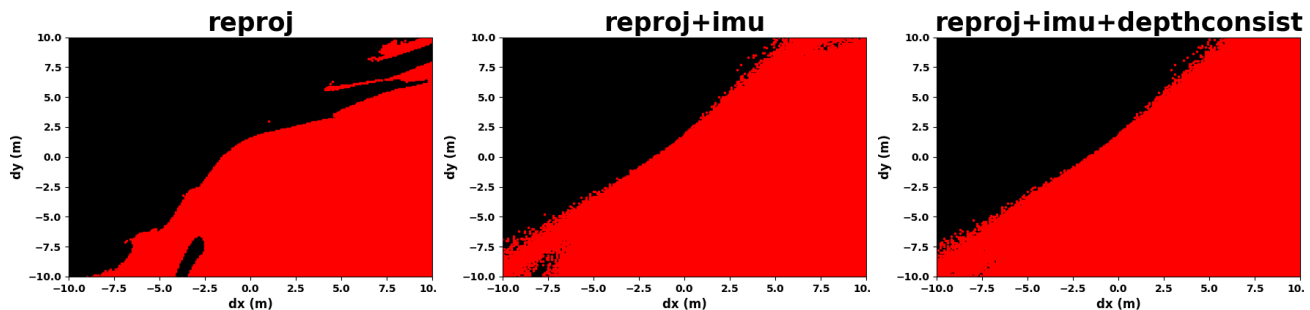


Fig. 24: The basin of attraction for **left**: visual BA, **center**: VI-BA, **right**: AB-VINS VI-BA with depth consistency. Converged points are in red, and diverged in black. It can be observed that the AB-VINS VI-BA converges the most often, making it the most robust optimization of the three.

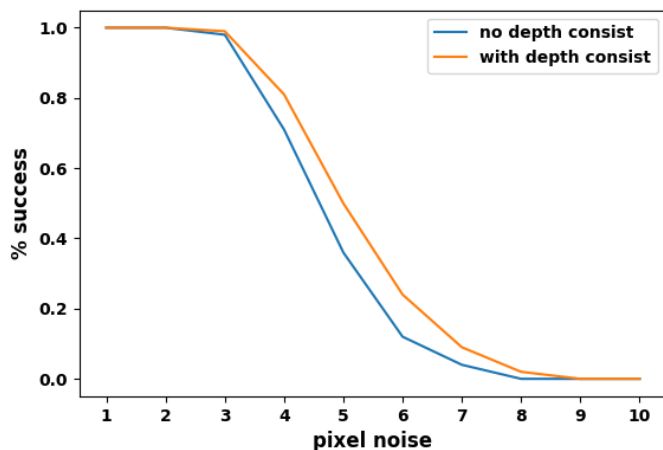


Fig. 25: Comparing the robustness to pixel noise for our VI-BA with depth consistency and a standard VI-BA.

only the position error is reported here since the orientation error is impossible to calculate for the static sequences, and SE(3) alignment is used instead of the typical 4-DoF alignment since it is impossible to estimate the transform between the motion capture frame and the gravity-aligned frame with no motion in the trajectory. It can be seen in Table VII that AB-VINS (both in the VIO and SLAM setting) is the only system that can successfully initialize and estimate the poses in all sequences. A system is determined to have failed in this experiment if there was no pose output (e.g., it did not attempt to initialize) or if the position error is over 10m. OKVIS and ORB-SLAM3 fail to initialize in any of the sequences, while OpenVINS is successful in the final two, and VINS-Fusion is successful in all but the first completely static sequence and the rotation-only sequence. The performance of VINS-Fusion is surprisingly very robust to low excitation for a completely hand-crafted system, but nevertheless AB-VINS can work in all of the scenarios.

We also provide visualizations of each trajectory in the dataset and the estimated trajectories for each system which successfully initialized. The plots are shown in Figs. 18, 19, 20, 21, 22, and 23 for the *static*, *semi-static*, *rotation*, *motion 1*, *motion 2*, and *motion 3* se-

TABLE VIII: Optimization with 40,401 different initials.

Optimization	# Success	% Success
V-BA	19177	47.5
VI-BA	24338	60.2
VI-BA + depth consist. (Ours)	24592	60.9

quences, respectively. For the *static* sequence in Fig. 18, AB-VINS is the only system which is able to initialize because of the lack of any motion at all. The scale of the plot is very small, which leads to a jagged appearance of the trajectories even though they are smooth from a distance. On the *semi-static* sequence in Fig. 19, VINS-Fusion is surprisingly able to initialize. However, it is clear from the z-axis time-series plot that it takes longer than AB-VINS to start up, since it requires at least a small amount of motion – which is present in a small amount in the z direction due to human error in trying to hold the device still. For the *rotation* sequence in Fig. 20, VINS-Fusion fails to initialize again. This is because the operator was able to hold the device more still in terms of translation than for the *semi-static* sequence, and rotation-only does not supply enough parallax for VINS-Fusion to triangulate features. On the *motion 1* sequence in Fig. 21, VINS-Fusion begins to noticeably produce a better trajectory than AB-VINS, since sufficient parallax is now present. However, it again takes longer to initialize – delaying the startup of any downstream application. For the *motion 2* and *motion 3* sequences in Figs. 22 and 23, OpenVINS is now able to initialize and produce reasonable results. However, again, the completely hand-crafted systems exhibit delayed initialization, while AB-VINS is able to start from the first frame. Despite there being more motion in the *motion 3* sequence than a typical AR/VR scenario, OKVIS and ORB-SLAM3 fail to initialize.

2) *Robustness of Local Mapping Optimization*: To investigate the robustness of our local mapping optimization, we turn to simulation. Using the *table 1* sequence of the AR Table dataset, we fit a BSpline to the trajectory. The derivatives of the BSpline are used to simulate IMU measurements, and 3D landmarks are generated randomly and projected to simulate feature track and scale-less inverse depth measurements. Cam-

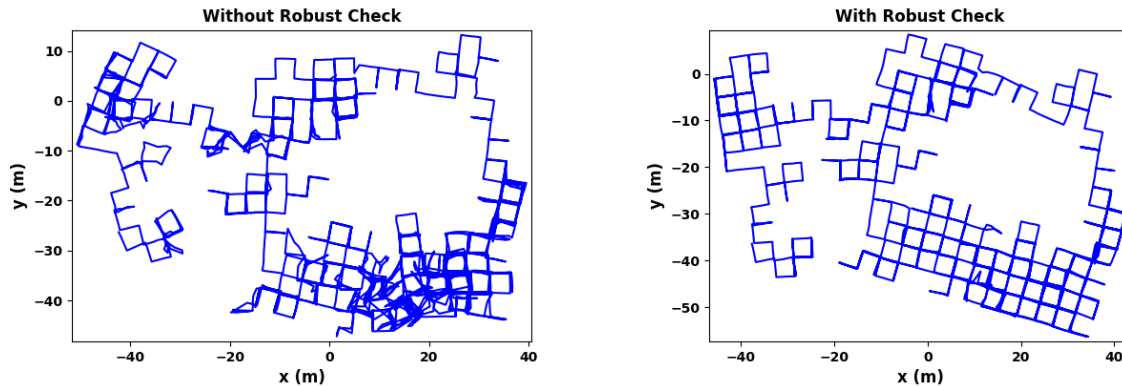


Fig. 26: The results of adding simulated bad loop measurements to the optimization. **Left:** the result without our robust χ^2 check. **Right:** the result with our robust check.

TABLE IX: Simulated IMU saturation over 1,000 trials.

Preintegration Method	# Success	% Success
Standard	8	0.8
Ours (robust)	953	95.3

era measurements are generated at 1Hz to simulate keyframes, and two keyframes along with the measurements are fed to our local mapping optimization.

We investigate the basin of attraction for the optimization with 1) only visual measurements (V-BA), 2) visual and inertial measurements (VI-BA), and 3) our full VI-BA with depth consistency. All feature parameters (3D landmarks and AB features) are fixed to the ground truth for this experiment. The initial guess of the second IMU position is perturbed over a 10×10 meter grid in increments of 0.1m in order to investigate the basin of attraction. The visual results are shown in Fig. 24, where it can be observed that the VI-BA is more robust than the V-BA, and our VI-BA with depth consistency is the most robust of the three. The number of successful runs is also reported in Table VIII. Success (the attraction set) is determined here if the estimated IMU position converged within 1cm of the ground truth.

We also investigate the robustness of local mapping to pixel noise. We run the simulation with pixel noise varying from 1 to 10 – averaged over 100 different random seeds per pixel noise. We compare our full VI-BA with depth consistency to the standard VI-BA. The results are shown in Fig. 25, where it can be seen that our VI-BA is more robust than the standard one. Note that the standard 1 pixel noise covariance value was provided to the estimators here, so the increased noise is unknown to the system.

3) *Robustness to IMU Saturation:* IMU saturation can occur during sharp motions or the sensors hitting into an object. While most VINS systems are not robust to IMU saturation, AB-VINS is. To show this, we ran the same simulation as in the previous section, but added saturated IMU measurements to a random axis for 1% of the simulated gyroscope and accelerometer measurements. We use the full VI-BA with depth consistency cost in this experiment. The simulation is

run with 1,000 different random seeds both with our robust method for IMU saturation (inflating the noise) and without. It can be seen in Table IX that our robust noise inflation method is successful nearly all of the time, while the standard method fails almost all of the time.

4) *Robustness to Bad Loops:* Bad loop closure detections (e.g., from incorrect place recognitions) are typically catastrophic for SLAM systems. On the other hand, our robust χ^2 check for loop measurements makes AB-VINS robust to bad loops that may make it past conventional measures to prevent them. To showcase this, using the M3500 dataset, we simulate bad loop measurements for 10% of the loops by adding large random noise to the yaw and position portions of the measurements (standard normal noise in radians for yaw and larger noise for position with standard deviation ranging from 1 to 50 randomly). The results can be seen in Fig. 26, where it can be observed that our robust χ^2 check successfully rejects the majority of bad loops, while not using the check results in a visibly worse trajectory. The memory tree top-down optimization method is used in both cases for this experiment.

V. CONCLUSION

We have presented a new visual-inertial SLAM system called AB-VINS, which utilizes three different deep networks. We showed that it is possible, in AB-VINS, to only estimate a and b for monocular depth maps, as well as some other terms (c and d) to correct the depth with multi-view information instead of each feature position separately. The memory tree, a novel data structure to speed up pose graph optimization, has been introduced. AB-VINS has been shown to have state-of-the-art robustness and efficiency, while also providing dense depth. AB-VINS is a different kind of VINS system – one that heavily relies on deep learning as well as new and improved hand-crafted techniques, and prioritizes efficiency and robustness over accuracy. With this new approach in the open, we hope that researchers can reshape how they do VINS.

VI. ACKNOWLEDGEMENT

We would like to thank Mingyang Li for his constant support and discussion throughout the development of AB-

VINS. We would also like to thank Yuxiang Peng, Saimouli Katragadda, and Chuchu Chen for their help in collecting the low/no excitation dataset. This work was partially supported by the University of Delaware (UD) College of Engineering, the NSF (IIS-1924897, MRI-2018905, SCH-2014264), and Google ARCore.

REFERENCES

- [1] R. Mur-Artal and J. D. Tardós, “Visual-inertial monocular SLAM with map reuse,” *IEEE Robotics and Automation Letters*, vol. 2, no. 2, pp. 796–803, 2017.
- [2] C. Campos, R. Elvira, J. J. Gomez, J. M. M. Montiel, and J. D. Tardós, “ORB-SLAM3: An accurate open-source library for visual, visual-inertial and multi-map SLAM,” *IEEE Transactions on Robotics*, vol. 37, no. 6, pp. 1874–1890, 2021.
- [3] T. Qin, P. Li, and S. Shen, “VINS-Mono: A robust and versatile monocular visual-inertial state estimator,” *IEEE Transactions on Robotics*, vol. 34, no. 4, pp. 1004–1020, 2018.
- [4] T. Schneider, M. T. Dymczyk, M. Fehr, K. Egger, S. Lynen, I. Gilitschenski, and R. Siegwart, “maplab: An open framework for research in visual-inertial mapping and localization,” *IEEE Robotics and Automation Letters*, 2018.
- [5] V. Usenko, N. Demmel, D. Schubert, J. Stückler, and D. Cremers, “Visual-inertial mapping with non-linear factor recovery,” *IEEE Robotics and Automation Letters*, vol. 5, no. 2, pp. 422–429, 2020.
- [6] S. Leutenegger, “OKVIS2: Realtime scalable visual-inertial slam with loop closure,” 2022.
- [7] A. I. Mourikis and S. I. Roumeliotis, “A multi-state constraint Kalman filter for vision-aided inertial navigation,” in *Proceedings of the IEEE International Conference on Robotics and Automation*, (Rome, Italy), pp. 3565–3572, Apr. 10–14, 2007.
- [8] M. Li and A. I. Mourikis, “Vision-aided inertial navigation for resource-constrained systems,” in *Proc. of the IEEE/RSJ International Conference on Intelligent Robots and Systems*, pp. 1056–1063, October 2012.
- [9] M. Li and A. I. Mourikis, “High-precision, consistent EKF-based visual-inertial odometry,” *International Journal of Robotics Research*, vol. 32, no. 6, pp. 690–711, 2013.
- [10] K. Wu, A. Ahmed, G. A. Georgiou, and S. I. Roumeliotis, “A square root inverse filter for efficient vision-aided inertial navigation on mobile devices,” in *Proc. of the Robotics: Science and Systems Conference*, 2015.
- [11] Z. Huai and G. Huang, “Robocentric visual-inertial odometry,” *International Journal of Robotics Research*, Apr. 2019.
- [12] S. Leutenegger, S. Lynen, M. Bosse, R. Siegwart, and P. Furgale, “Keyframe-based visual-inertial odometry using nonlinear optimization,” *International Journal of Robotics Research*, 2014.
- [13] A. Rosinol, M. Abate, Y. Chang, and L. Carlone, “Kimera: an open-source library for real-time metric-semantic localization and mapping,” in *IEEE Intl. Conf. on Robotics and Automation (ICRA)*, 2020.
- [14] X. Zuo, N. Merrill, W. Li, Y. Liu, M. Pollefeys, and G. Huang, “CodeVIO: Visual-inertial odometry with learned optimizable dense depth,” in *Proc. of the IEEE International Conference on Robotics and Automation*, (Xi’an, China), 2021.
- [15] M. Zhao, D. Zhou, X. Song, X. Chen, and L. Zhang, “DiT-SLAM: real-time dense visual-inertial slam with implicit depth representation and tightly-coupled graph optimization,” *Sensors*, vol. 22, no. 9, p. 3389, 2022.
- [16] Y. Xin, X. Zuo, D. Lu, and S. Leutenegger, “SimpleMapping: Real-Time Visual-Inertial Dense Mapping with Deep Multi-View Stereo,” in *IEEE International Symposium on Mixed and Augmented Reality (ISMAR)*, Oct 2023.
- [17] R. A. Newcombe, S. J. Lovegrove, and A. J. Davison, “DTAM: Dense tracking and mapping in real-time,” in *2011 international conference on computer vision*, pp. 2320–2327, IEEE, 2011.
- [18] L. Koestler, N. Yang, N. Zeller, and D. Cremers, “TANDEM: Tracking and dense mapping in real-time using deep multi-view stereo,” in *5th Annual Conference on Robot Learning*, 2021.
- [19] K. Tateno, F. Tombari, I. Laina, and N. Navab, “CNN-SLAM: Real-time dense monocular slam with learned depth prediction,” in *Proceedings of the IEEE Conference on Computer Vision and Pattern Recognition*, pp. 6243–6252, 2017.
- [20] C. Tang and P. Tan, “Ba-net: Dense bundle adjustment network,” 2019.
- [21] M. Bloesch, J. Czarnowski, R. Clark, S. Leutenegger, and A. J. Davison, “CodeSLAM—learning a compact, optimisable representation for dense visual slam,” in *Proceedings of the IEEE conference on computer vision and pattern recognition (CVPR)*, pp. 2560–2568, 2018.
- [22] J. Czarnowski, T. Laidlow, R. Clark, and A. J. Davison, “Deepfactors: Real-time probabilistic dense monocular slam,” *IEEE Robotics and Automation Letters*, vol. 5, no. 2, pp. 721–728, 2020.
- [23] R. Ranftl, K. Lasinger, D. Hafner, K. Schindler, and V. Koltun, “Towards robust monocular depth estimation: Mixing datasets for zero-shot cross-dataset transfer,” *IEEE Transactions on Pattern Analysis and Machine Intelligence*, vol. 44, no. 3, 2022.
- [24] K. Konolige, G. Grisetti, R. Kummerle, W. Burgard, B. Limketkai, and R. Vincent, “Efficient sparse pose adjustment for 2D mapping,” in *Proc. of the IEEE/RSJ International Conference on Intelligent Robots and Systems*, pp. 22–29, 2010.
- [25] M. Kaess, A. Ranganathan, and F. Dellaert, “iSAM: Incremental smoothing and mapping,” *IEEE Transactions on Robotics*, vol. 24, pp. 1365–1378, 2008.
- [26] M. Kaess, H. Johannsson, R. Roberts, V. Ila, J. J. Leonard, and F. Dellaert, “iSAM2: Incremental smoothing and mapping using the bayes tree,” *The International Journal of Robotics Research*, vol. 31, pp. 216–235, 2011.

- [27] G. Sibley, C. Mei, I. Reid, and P. Newman, “Adaptive relative bundle adjustment,” in *Proc. Robotics: Science and Systems (RSS)*, 2010.
- [28] N. Merrill, P. Geneva, S. Katragadda, C. Chen, and G. Huang, “Fast monocular visual-inertial initialization leveraging learned single-view depth,” in *Proc. Robotics: Science and Systems (RSS)*, 2023.
- [29] Y. Zhou, A. Kar, E. Turner, A. Kowdle, C. X. Guo, R. C. DuToit, and K. Tsotsos, “Learned Monocular Depth Priors in Visual-Inertial Initialization,” in *European conference on computer vision*, 2022.
- [30] B. D. Lucas and T. Kanade, “An iterative image registration technique with an application to stereo vision,” in *Proceedings of the 7th International Joint Conference on Artificial Intelligence - Volume 2, IJCAI’81*, (San Francisco, CA, USA), p. 674–679, Morgan Kaufmann Publishers Inc., 1981.
- [31] E. Rosten and T. Drummond, “Machine learning for high-speed corner detection,” in *Computer Vision – ECCV 2006*, (Berlin, Heidelberg), pp. 430–443, Springer Berlin Heidelberg, 2006.
- [32] N. Trawny and S. I. Roumeliotis, “Indirect Kalman filter for 3D attitude estimation,” tech. rep., University of Minnesota, Dept. of Comp. Sci. & Eng., Mar. 2005.
- [33] T. Lupton and S. Sukkarieh, “Visual-inertial-aided navigation for high-dynamic motion in built environments without initial conditions,” *IEEE Transactions on Robotics*, vol. 28, no. 1, pp. 61–76, 2012.
- [34] C. Forster, L. Carlone, F. Dellaert, and D. Scaramuzza, “Imu preintegration on manifold for efficient visual-inertial maximum-a-posteriori estimation,” in *Robotics: Science and Systems XI*, 2015.
- [35] K. Eickenhoff, P. Geneva, and G. Huang, “Closed-form preintegration methods for graph-based visual-inertial navigation,” *International Journal of Robotics Research*, vol. 38, no. 5, pp. 563–586, 2019.
- [36] R. Ranftl, A. Bochkovskiy, and V. Koltun, “Vision transformers for dense prediction,” *ICCV*, 2021.
- [37] Z. Liu, Y. Lin, Y. Cao, H. Hu, Y. Wei, Z. Zhang, S. Lin, and B. Guo, “Swin transformer: Hierarchical vision transformer using shifted windows,” in *Proceedings of the IEEE/CVF International Conference on Computer Vision (ICCV)*, pp. 10012–10022, October 2021.
- [38] J. Kannala and S. Brandt, “A generic camera model and calibration method for conventional, wide-angle, and fish-eye lenses,” *IEEE Transactions on Pattern Analysis and Machine Intelligence*, vol. 28, no. 8, pp. 1335–1340, 2006.
- [39] R. Arandjelovic, P. Gronát, A. Torii, T. Pajdla, and J. Sivic, “NetVLAD: CNN architecture for weakly supervised place recognition,” in *Proceedings of the IEEE conference on computer vision and pattern recognition (CVPR)*, pp. 5297–5307, 2016.
- [40] D. DeTone, T. Malisiewicz, and A. Rabinovich, “SuperPoint: Self-supervised interest point detection and description,” in *CVPR Deep Learning for Visual SLAM Workshop*, 2018.
- [41] B. Horn, H. Hilden, and S. Negahdaripour, “Closed-form solution of absolute orientation using orthonormal matrices,” *Journal of the Optical Society of America A*, vol. 5, pp. 1127–1135, 07 1988.
- [42] M. AdelsonVelskii and E. M. Landis, “An algorithm for the organization of information,” tech. rep., JOINT PUBLICATIONS RESEARCH SERVICE WASHINGTON DC, 1963.
- [43] P. Geneva, K. Eickenhoff, W. Lee, Y. Yang, and G. Huang, “OpenVINS: a research platform for visual-inertial estimation,” in *Proc. of the IEEE International Conference on Robotics and Automation*, (Paris, France), 2020.
- [44] S. Agarwal, K. Mierle, and T. C. S. Team, “Ceres Solver,” 10 2023.
- [45] C. Chen, P. Geneva, Y. Peng, W. Lee, and G. Huang, “Monocular visual-inertial odometry with planar regularity,” in *Proc. of the IEEE International Conference on Robotics and Automation*, 2023.
- [46] D. Schubert, T. Goll, N. Demmel, V. Usenko, J. Stückler, and D. Cremers, “The TUM VI benchmark for evaluating visual-inertial odometry,” in *2018 IEEE/RSJ International Conference on Intelligent Robots and Systems (IROS)*, pp. 1680–1687, IEEE, 2018.
- [47] F. Dellaert and G. Contributors, “borglab/gtsam,” May 2022.